Reviews in Mineralogy & Geochemistry
Vol. 86 pp. 401–428, 2021

Triple Oxygen Isotope Systematics in the Hydrologic Cycle

Jakub Surma
Institute of Geology and Mineralogy
University of Cologne
Zülpicher Straße 49b
Cologne, 50674
Germany
jakub.surma@uni-goettingen.de

presently at:
Geoscience Center
Georg August University
Goldschmidtstraße 1
Göttingen, 37077
Germany

Sergey Assonov
formerly at:
Institute of Geology and Mineralogy
University of Cologne
Zülpicher Straße 49b
Cologne, 50674
Germany

Michael Staubwasser
Institute of Geology and Mineralogy
University of Cologne
Zülpicher Straße 49b
Cologne, 50674
Germany

INTRODUCTION

The analysis of hydrogen (δD) and oxygen ($\delta^{18}O$) isotope ratios of H_2O are widely used tools for studies of the hydrological cycle (Friedman 1953; Dansgaard 1954; Gonfiantini 1986; Gat 1996; Araguás-Araguás et al. 2000; Gat et al. 2000) and climate reconstruction (Dansgaard 1964; Johnsen et al. 1989; Petit et al. 1999). Natural variations of δD and $\delta^{18}O$ in precipitation are well correlated and fall on a common global trend, the Global Meteoric Water Line (GMWL, Craig 1961):

$$\delta D = 8 \cdot \delta^{18}O + 10‰ \quad (1)$$

The slope (λ^2_{GMWL}) of 8 in this equation is defined by mass-dependent equilibrium fractionation during condensation of atmospheric vapor (Dansgaard 1964; Horita and Wesolowski 1994).

1529-6466/21/0086-0012$05.00 (print)
1943-2666/21/0086-0012$05.00 (online)
http://dx.doi.org/10.2138/rmg.2021.86.12

The 10‰ positive offset in δD results from kinetic (diffusive) isotope fractionation during the initial formation of atmospheric vapor over the ocean which follows a slightly lower $\delta D/\delta^{18}O$ slope than the GWML (Craig and Gordon 1965; Merlivat 1978). Typically, any evaporation process in the hydrologic cycle results in waters that deviate from the average global λ^{2}_{GMWL}. This deviation is expressed with the d-excess parameter (e.g., Gat 1996):

$$\text{d-excess} = \delta D - 8 \cdot \delta^{18}O \tag{2}$$

The process of isotopic fractionation during vapor formation is explained by the evaporation model of Craig and Gordon (1965) (Fig. 1). The model describes the total isotopic fractionation ($^{*}\alpha_{L-V-evap}$) resulting from evaporation from a water body ($^{*}R_W$), which is controlled by relative humidity (*h*), fractionation factors for equilibrium and diffusion, and the isotopic composition of free atmospheric vapor ($^{*}R_A$). At lower *h*, the vapor concentration gradient between the interface layer (vapor saturation) and the free atmosphere increases and amplifies diffusivity. Hence, the magnitude of d-excess is mostly controlled by relative humidity (*h*) and becomes larger when *h* decreases (Craig and Gordon 1965; Cappa et al. 2003; Steen-Larsen et al. 2014). Therefore, d-excess is traditionally used to reconstruct evaporation conditions at vapor source regions and to quantify evaporation of continental water bodies (Gat and Bowser 1991; Gat 1996; Masson-Delmotte et al. 2005; Pfahl and Wernli 2008).

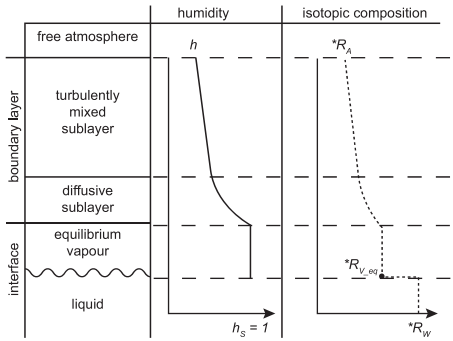

Figure 1. The Craig and Gordon Model for evaporation of surface water (modified from Gat 1996).

However, the d-excess parameter is not exclusively controlled by *h* but also by the different temperature sensitivity of equilibrium fractionation factors for D/H ($^{2}\alpha_{L-V-eq}$) and $^{18}O/^{16}O$ ($^{18}\alpha_{L-V-eq}$). This prevents a unique interpretation by introducing uncertainty to *h* estimates (Horita and Wesolowski 1994; Luz et al. 2009). Also, the diffusivity fractionation factors ($^{2}\alpha_{diff}$ and $^{18}\alpha_{diff}$, respectively) of both isotope systems underlie a temperature dependent relationship (Luz et al. 2009):

$$^{2}\alpha_{diff} = \left(1.25 - 0.02 \cdot T\right) \cdot \left(^{18}\alpha_{diff} - 1\right) + 1 \tag{3}$$

Due to the different temperature relationships of D/H and $^{18}O/^{16}O$ fractionation factors for liquid–vapor and solid–vapor equilibrium ($^{2}\alpha_{S-V-eq}$ and $^{18}\alpha_{S-V-eq}$, respectively), d-excess is additionally affected by precipitation temperature (Merlivat and Nief 1967; Majoube 1971; Ellehoj et al. 2013). The additional combined analysis of $^{17}O/^{16}O$ and $^{18}O/^{16}O$ of H_2O was suggested to be a promising complement to reconstruct relative humidity at the vapor source (Angert et al. 2004).

Analysis

Due to methodical limitations and analytical uncertainties, the use of triple oxygen isotopes in hydrological applications was impractical in the past. However, the temperature dependency

of d-excess created the need for another second order parameter of water isotopologues. In parallel, methodical advances over the past two decades provided the necessary analytical resolution to identify mass-dependent anomalies in the ^{16}O–^{17}O–^{18}O distribution in natural waters (Meijer and Li, 1998; Baker et al. 2002). The latter method was greatly advanced by Barkan and Luz (2005). An analytical uncertainty of ±0.005‰ for ^{17}O-excess was achieved based on liberation of oxygen gas from H_2O by means of fluorination with a CoF_3 reagent, providing an adequate precision to resolve small variations in the hydrosphere and to determine $H_2{}^{17}O/H_2{}^{16}O$ equilibrium and diffusivity fractionation factors ($^{17}\alpha_{L-V-eq}$ and $^{17}\alpha_{diff}$, respectively) with a sufficient accuracy (Barkan and Luz 2005, 2007). Over the past decade, laser absorption instruments have been developed and also proven to achieve sufficiently high precision to resolve ^{17}O-excess variations in natural waters (Berman et al. 2013; Steig et al. 2014; Affolter et al. 2015; Schauer et al. 2016; Tian et al. 2016).

Analytical requirements: Two-point calibration. Reported $\delta^{18}O$ in natural waters so far ranges from −69.6‰ (East Antarctic snow) to 29.2‰ (Sistan Desert, Iran) and, thus, covers a total range of approximately 100‰ (Surma et al. 2015; Touzeau et al. 2016). In order to account for inter-laboratory scaling differences, a two-point calibration based on certified reference materials is essential (e.g., Kaiser 2008; Kusakabe and Matsuhisa 2008). A commonly used normalization in triple oxygen isotope studies is the one suggested by Schoenemann et al. (2013):

$$\delta^* O_{smp\_VSMOW-SLAP} = \delta^* O_{smp\_VSMOW} \cdot \frac{\delta^* O^{nom}_{SLAP/VSMOW}}{\delta^* O^{meas}_{SLAP/VSMOW}} \quad (4)$$

where $\delta^* O_{smp\_VSMOW}$ is the measured value of a sample expressed against VSMOW, $\delta^* O^{nom}_{SLAP/VSMOW}$ is the assigned distance between SLAP–2 and VSMOW–2, and $\delta^* O^{meas}_{SLAP/VSMOW}$ is the difference between SLAP–2 and VSMOW–2 in the respective laboratory. Assigned values for SLAP–2 (vs. VSMOW–2) are $\delta^{17} O^{nom}_{SLAP/VSMOW} = -29.6986‰$ and $\delta^{18} O^{nom}_{SLAP/VSMOW} = -55.5‰$ (^{17}O-excess = 0 per meg).

New data presented in this work

This review is supplemented with new samples and data from one case study in the high-altitude environment of the Southern German Alps. Sampling was carried out at Mt. Zugspitze (2962 m above sea level, m a.s.l.), 10 km SW of Garmisch-Partenkirchen (720 m a.s.l.). The temperate regional climate is characterized by a mean annual temperature of −4.3 °C. Samples were collected from February to May 2016 in the local surrounding of Mt. Zugspitze—at the Schneefernerhaus Research Station (UFS, 2,650 m a.s.l.) and the nearby Zugspitze plateau (Zugspitzplatt, N 10.99°, E 47.41°; ~2,450 m a.s.l.). The sample set comprises 25 atmospheric vapor samples (Table S1) that were collected in February and May 2016 by means of cryogenic extraction at UFS station in LN_2 at low pressure in a modified version of a high efficiency trap (Brenninkmeijer and Röckmann 1996). We also obtained a total number of 25 precipitation/snow samples and a larger number of samples from the seasonal local snow cover (Tables S2 and S3).

Isotope analysis. All samples were analyzed for their triple oxygen isotope and hydrogen isotope composition at the Institute for Geology and Mineralogy, University of Cologne. $^{17}O/^{16}O$ and $^{18}O/^{16}O$ analysis is performed with modified method based on Barkan and Luz (2005). Details on the analytical procedure are given in Surma et al. (2015, 2018). Long-term external reproducibility of standard waters and selected samples is approx. ±0.06‰ ($\delta^{17}O$), ±0.1‰ ($\delta^{18}O$), and ±8 per meg (^{17}O-excess). D/H ratios were determined by continuous flow analysis of H_2 gas liberated by TC/EA carbon reduction of H_2O at 1550 °C (also see Surma et al. 2018). The average long-term external reproducibility is approximately ±0.3‰ for δD and ±2.1‰ for d-excess. Laboratory reference waters were analyzed between every 5 to 10 samples. All isotope data were normalized to the SMOW-SLAP scale following the procedure suggested by Schoenemann et al. (2013) and standard-sample bracketing (Table S4).

TRIPLE OXYGEN ISOTOPES IN WATER

Triple oxygen isotope fractionation

The triple oxygen isotope fractionation exponent for equilibrium liquid–vapor fractionation (θ_{L-V-eq}) was determined by Barkan and Luz (2005), giving a constant θ_{L-V-eq} of 0.529 for the entire experimental T range from 11.4 to 41.5 °C. Therefore, ^{17}O-excess can be considered temperature-independent for equilibrium fractionation of evaporation from water surfaces and formation of rain. A difficulty arises from the fact that no experimental data are available for triple oxygen isotope fractionation at solid–vapor equilibrium of H_2O. Theoretical predictions suggest $\theta_{S-V-eq} \approx 0.528$ (Van Hook 1968). Landais et al. (2012b) confirm this value with a set of vapor and snowfall samples from Greenland.

Molecular diffusion of water vapor in air is characterized by a somewhat lower θ_{diff} of 0.5185 ± 0.0002 (Barkan and Luz 2007). However, the experiment has shown a small temperature dependence in the range from 0.5183 ± 0.0001 (25 °C) to 0.5187 ± 0.0001 (40 °C). It is unclear whether this θ_{diff}/T trend is linear and whether a lower θ_{diff} would apply for diffusive fractionation at low temperatures (e.g., 0.5172 at −50 °C if the trend is extrapolated linearly; Bao et al. 2016).

^{17}O-excess during the formation of vapor

In the field of hydrology ^{17}O-excess is the commonly used term to describe deviations of $^{17}O/^{16}O$ ratios from a reference slope with $\lambda^{17}_{GMWL} = 0.528$ and typically reported in per meg with respect to VSMOW (Meijer and Li, 1998; Luz and Barkan 2010):

$$^{17}\text{O-excess (per meg)} = (\delta'^{17}\text{O} - 0.528 \cdot \delta'^{18}\text{O}) \cdot 10^6 \quad (5)$$

with $\delta'^{*}\text{O} = \ln(\delta^{*}\text{O}+1)$. λ^{17}_{GMWL} here is defined by the slope of average global precipitation—represented by the Global Meteoric Water Line—in the δ'^{17}O vs. δ'^{18}O space. The GMWL itself shows a positive offset of ~33 per meg with respect to seawater (Luz and Barkan 2010).

The exact magnitude—or slope (Fig. 2)—of $^{*}\alpha_{L-V-evap}$ is determined by h, respective equilibrium and diffusion fractionation factors, and the isotopic composition of vapor in the free atmosphere (cf. Fig. 1; Craig and Gordon 1965; Ehhalt and Knott 1965; Criss 1999; Cappa et al. 2003):

$$^{*}\alpha_{L\text{-}V\_evap} = \frac{^{*}\alpha_{diff} \cdot {}^{*}\alpha_{L\text{-}V\_eq} \cdot (1-h)}{1 - {}^{*}\alpha_{L\text{-}V_{eq}} \cdot h \cdot \left({}^{*}R_A / {}^{*}R_W \right)} \quad (6)$$

For a single moisture source (e.g., open ocean) and absence of vapor admixture, all atmospheric vapor is generated from the evaporating water itself and $^{*}R_V = {}^{*}R_V$ (closure assumption). In that case Equation (6) reduces to:

$$^{*}\alpha_{L\text{-}V\_evap} = {}^{*}\alpha_{L\text{-}V\_eq} \cdot \left({}^{*}\alpha_{diff} \cdot (1-h) + h \right) \quad (7)$$

The temperature of ambient air may deviate from the temperature of the water surface in natural settings. Here, normalized humidity (h_n) should be used in Equations (6) and (7) instead of h. h_n is calculated by:

$$h_n = h \cdot \frac{q_{sat\_a}}{q_{sat\_s}} \quad (8)$$

where q_{sat_a} is the vapor concentration in the free air and q_{sat_s} is the saturated vapor concentration at water temperature (Barkan and Luz 2007; Uemura et al. 2010).

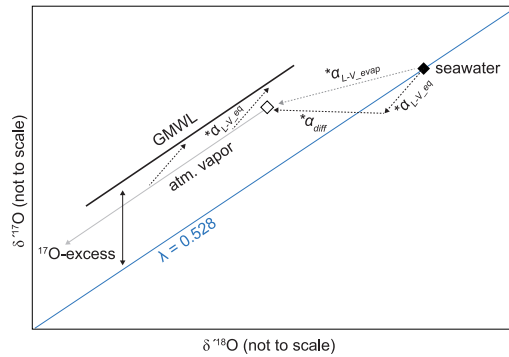

Figure 2. Fractionation of triple oxygen isotopes in the atmosphere (modified from Barkan and Luz 2007). Initial atmospheric vapor (**white diamond**) forms from sea water (**black diamond**) at non-equilibrium conditions. Evaporation results in positive lower $\delta'^{17}O$ and $\delta'^{18}O$, and higher ^{17}O-excess of vapor with respect to the reference slope (**blue**). Transport, cooling, and rainout leads to steady isotopic depletion of the residual vapor reservoir.

In addition, air turbulence—or wind—reduce the magnitude of diffusive isotope fractionation during the evaporation process. In the Craig and Gordon Model, this effect is described by the turbulently mixed sublayer, in which actual mixing of air with different vapor concentration balances the *h* gradient without molecular diffusion (Fig. 1). However, the derivation of a clear relationship between wind speed and lowering of molecular diffusion is complex (Merlivat and Jouzel 1979). A recent study demonstrates that, we cite: '*for isotope water balance studies where winds are frequently above 2 m/s, the C–G model may be inadequate without appropriate corrections for spray vaporization, or the introduction of appropriate kinetic isotope fractionation factors*' (Gonfiantini et al. 2020). This would be strongest felt over water bodies deep enough to sustain breaking waves. In order to account for boundary layer turbulence, the effect is usually parametrized in the Craig and Gordon model by correcting $^*\alpha_{diff}$ with the exponent *n*:

$$^*\alpha_{diff(corr)} = \left(^*\alpha_{diff}\right)^n \tag{9}$$

n is determined empirically and ranges from 1 (pure molecular diffusion) to 0.5 (rough continental regime) (Dongmann et al. 1974; Mathieu and Bariac 1996; Haese et al. 2013). Reduction of diffusive fractionation with $n < 0.5$ is observed for wind tunnel experiments and evaporation above the ocean surface (Merlivat and Jouzel 1979; Uemura et al. 2010).

NATURAL VARIATIONS OF ^{17}O-EXCESS IN WATER

Meaning and purpose of the Global Meteoric Water Line

δD and $\delta^{18}O$ in meteoric waters around the world are tightly correlated and follow the $\delta D/\delta^{18}O$ trend (λ^2) with a slope of 8 (Eqn. 1), i.e., the GMWL (Craig 1961; Dansgaard 1964). The +10‰ offset (d-excess) results from diffusive, non-equilibrium fractionation during formation of pristine vapor above the ocean (Eqn. 6), resulting in relative preferential enrichment of deuterium with respect to ^{18}O in the vapor phase. Precipitation that forms from that vapor follows the GMWL towards more depleted values with increasing distance from the coast, higher latitude, and increasing altitude, whereby the underlying process is approximated by Rayleigh distillation (Dansgaard 1964; Horita et al. 2008). The GMWL concept provides an empirical reference frame for the field of stable isotope hydrology, but is in general agreement with Rayleigh fractionation (Dansgaard 1964; Criss 1999).

Meijer and Li (1998) analyzed a set of natural waters yielding $\lambda^{17}_{GMWL} = 0.528$, thus providing an analogous reference frame for $^{17}O/^{16}O$ and $^{18}O/^{16}O$. Including standard measurements of GISP, SLAP, and Antarctic snow data (Barkan and Luz 2005; Landais et al. 2008) to their larger dataset of natural waters ($n = 52$), Luz and Barkan (2010) confirmed this slope for the GMWL with a positive offset of 0.033‰ with respect to VSMOW–2:

$$\delta'^{17}O = 0.528 \cdot \delta'^{18}O + 0.033‰ \quad (10)$$

Similar to d-excess, the deviation from this line is reported as ^{17}O-excess (cf. Eqn. 5). The value of $\lambda^{17}_{GMWL} = 0.528$ is close to $\theta_{L-V\_eq} = 0.529$, thus confirming Rayleigh equilibrium condensation as the controlling mechanism of precipitate formation (Passey and Levin 2021, this volume). Figure 3 shows a compilation of reported triple oxygen isotope data of global precipitation, surface water bodies, hydrothermal waters, and seawater, that cover a total range of ≈ 100‰ in $\delta^{18}O$. In the case of closure ($^*R_{V_0} = {}^*R_{A_0}$, cf. Eqn. 7), vapor isotopic composition ($^*R_{V_0}$) is calculated by (Craig and Gordon 1965):

$${}^*R_{V_0} = {}^*R_{W_0} \cdot \frac{1}{{}^*\alpha_{L\text{-}V\_eq} \cdot \left({}^*\alpha_{diff} + h \cdot \left(1 - {}^*\alpha_{diff}\right)\right)} \quad (11)$$

where $^*R_{W_0}$ is the isotopic composition of ocean surface water. When the air parcel is advected and cooled after initial vapor formation, first condensate forms in equilibrium with $^*R_{V_0}$:

$${}^*R_{P_0} = {}^*R_{V_0} \cdot {}^*\alpha_{L\text{-}V\_eq} \quad (12)$$

The residual fraction (f_{res}) of initial oceanic vapor decreases with increasing distance from the source. The isotopic composition of residual vapor is calculated by the Rayleigh equation:

$${}^*R_A = {}^*R_{V_0} \cdot f_{res}^{{}^*\alpha_{L\text{-}V\_eq} - 1} \quad (13)$$

Precipitating water in equilibrium results in observed $\lambda^2_{GMWL} = 8$ and $\lambda^{17}_{GMWL} = 0.528$. For the triple oxygen isotope space this slope is valid for $\delta^{18}O$ ranges between –40‰ and –5‰ (Fig. 3), thus providing a reasonable reference frame for global precipitation that is mostly provided by Rayleigh distillation of oceanic vapor (e.g., Trenberth et al. 2007).

The bell-shaped distribution of ^{17}O-excess vs. $\delta^{18}O$ indicates that water samples found in the lower range of the $\delta^{18}O$ scale (polar snow) as well as in highly enriched samples (surface waters from arid regions) are systematically lower in ^{17}O-excess with respect to the GMWL (Fig. 3). We note that the apparent bell-shape to some degree may also result from a bias towards samples that are studied precisely because of their inherent kinetic fractionation effects found in polar and hyper-arid regions. The vast majority of continental waters not too far removed from the ocean source will likely fall in the $\delta^{18}O$ range from –30‰ to –5‰.

In the case of polar snow, the systematic deviation from the GMWL leads to pronounced Local Meteoric Water Lines (LMWL) > 0.528—i.e., showing positive correlation of ^{17}O-excess and $\delta^{18}O$—that result from snow formation at vapor supersaturation, and thus kinetic fractionation, at temperatures below –20 °C (Landais et al. 2012a,b; Casado et al. 2016). Miller (2018) states that this pattern of snow with $\delta^{18}O$ below –40‰ is also a result of 'diamond dust' (open-sky precipitation) contribution to central Antarctic snow cover, which is characterized by a fractionation slope of $\lambda^{17} = 0.531$ in this study. It is also suggested that the LMWL in remote polar regions may be additionally affected by incorporation of mass-independently, fractionated, largely ^{17}O-enriched stratospheric oxygen in precipitation (Winkler et al. 2013; Miller 2018). Evidence for stratospheric water intrusions is suggested by negative correlation of ^{17}O-excess and $\delta^{18}O$ found in the study which contradict the general synoptic

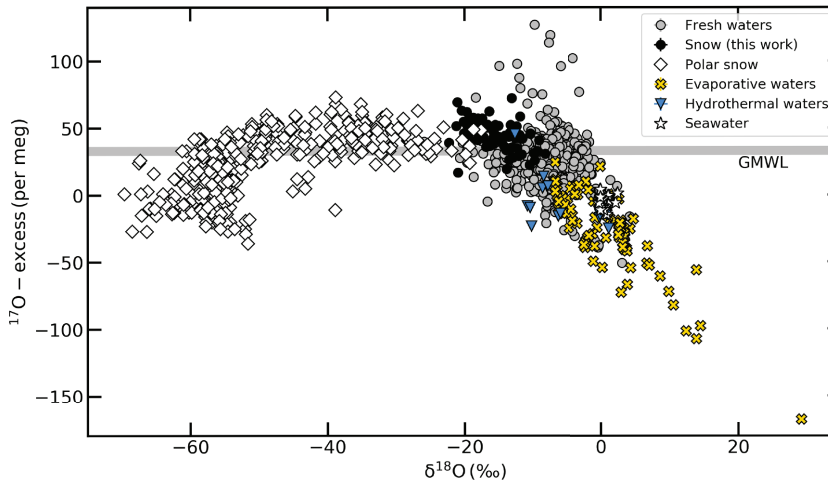

Figure 3. Compilation of ^{17}O-excess vs. δ^{18}O in global waters. The gray horizontal line depicts the GMWL as reported by Luz and Barkan (2010). Precipitation in polar regions (**diamonds**) show values below −24‰ in δ^{18}O. ^{17}O-excess ranges from 30 to 70 per meg in snow from Greenland and Alert, Canada, and shows correlation with decreasing δ^{18}O (below −40‰) for Antarctic precipitation (Landais et al. 2008, 2012a,b; Lin et al. 2013a; Winkler et al. 2013; Pang et al. 2015, 2019; Touzeau et al. 2016). Fresh waters (**gray circles**) comprise snowfall, rain, cave drip water, tap water, lakes, springs, and rivers (Landais et al. 2010; Luz and Barkan 2010; Lin et al. 2013a; Affolter et al. 2015; Li et al. 2015, 2017; Gázquez et al. 2018; Tian et al. 2018; Alexandre et al. 2019; Passey and Ji, 2019; Tian et al. 2019; Uechi and Uemura 2019; Bergel et al. 2020; Bershaw et al. 2020; Sha et al. 2020; Voigt et al. 2020; this study). In general, those waters range from −22‰ to ~0‰ in δ^{18}O and show a large variability in ^{17}O-excess, ranging from −40 to 120 per meg. Water bodies from arid, evaporative environments (**yellow crosses**) generally show δ^{18}O values higher than −8‰ and progressively lower ^{17}O-excess with increasing δ^{18}O. Lowest ^{17}O-excess values are found in highly evaporated water bodies from the Sistan Desert, Iran, the Atacama Desert, Chile, and Lake Chichancanab, Mexico (Surma et al. 2015, 2018; Evans et al. 2018; Voigt et al. 2020). Hydrothermal waters (**blue triangles**) are in good agreement with freshwaters and show a narrow range in δ^{18}O from −12‰ to −6‰ and from −20 to 45 per meg in ^{17}O-excess (Sharp et al. 2016; Wostbrock et al. 2018; Zakharov et al. 2019b). Seawater measurements are indicated with asterisks (Luz awnd Barkan 2010).

positive correlation in Antarctic precipitation. We note that such effects at mid-latitudes, which is the major focus of this review, are much less likely. First, stratospheric air is brought to the troposphere mostly by the polar vortex. The stratosphere-troposphere exchange flux at mid-latitudes is very limited. Second, the troposphere in the mid-latitudes has a much higher water content than the polar troposphere, so the mass-balance may be too unfavorable to observe stratospheric downdraft. Third, ^{17}O-excess found in snow at polar regions demonstrates only limited deviations, if any, from the range expected (Landais et al. 2012a; Touzeau et al. 2016).

Isotopically enriched samples from arid regions do not reflect fractionation effects during precipitate formation but a systematic decrease of ^{17}O-excess during intensive evaporation of continental waters (Surma et al. 2015, 2018; Voigt et al. 2020). Here the negative correlation of ^{17}O-excess and δ^{18}O in those waters is the result of excessive evaporation, where total fractionation integrated over the course of a day is controlled by relative humidity, evaporation degree, and evaporative loss with respect to recharge. Resulting trajectories in the δ'^{17}O vs. δ'^{18}O space are flatter than $\lambda^{17}_{\mathrm{GMWL}}$ and analog to local evaporation lines (LEL) known in the traditional δD vs. δ^{18}O system (Fontes and Gonfiantini 1967; Gat 1984; Gat and Bowser 1991). However, it should be noted that triple oxygen isotopes in natural evaporative systems do not depict straight lines but typically form curved trajectories.

^{17}O-excess in polar snow precipitation. Ice cores from Greenland and Antarctica are important records of past climate over glacial-interglacial cycles (e.g., Petit et al. 1999; NorthGRIP members 2004). The d-excess parameter is widely used to reconstruct variations in temperature and relative humidity at oceanic moisture sources (e.g., Vimeux et al. 1999; Steen-Larsen et al. 2011). However, the use of ^{17}O-excess shows promise as a novel and more robust temperature independent tracer that provides additional constraints on source region humidity (Uemura et al. 2010).

Landais et al. (2012b) investigated seasonal triple oxygen isotope variations in surface snow at the NEEM drilling site, Greenland, where a slight anticorrelation of δ^{18}O and ^{17}O-excess in snow is found. Maximum ^{17}O-excess is present in samples with lowest δ^{18}O values. Measurements of ^{17}O-excess and δ^{18}O in atmospheric vapor and concomitant snow at NEEM site show similar values in both phases that were also found to be in equilibrium based on previous δ^{18}O and δD measurements (Steen-Larsen et al. 2011; Landais et al. 2012b). Modeling of air temperature and relative humidity in moisture source regions also reveals that ^{17}O-excess reflects *h* conditions at the vapor source. Triple oxygen isotope studies on Greenland ice cores further provide valuable information on the coupling between high-latitude and low- to mid-latitude climate variations in the northern hemisphere during abrupt climatic changes over the course of the last glaciation (Guillevic et al. 2014; Landais et al. 2018).

For the case of Antarctica, Winkler et al. (2012) demonstrate that moisture source humidity can be reliably reconstructed from coastal ice core records, whereas the isotopic composition of snow in continental areas is dominated by local temperature effects. This is also confirmed by a spatial gradient which is observed for ^{17}O-excess in precipitation across Antarctica (Fig. 3), showing elevated values in coastal areas that are dominated by marine conditions and low ^{17}O-excess in the Antarctic interior (Landais et al. 2012a; Schoenemann et al. 2014; Touzeau et al. 2016). Low ^{17}O-excess in continental Antarctic precipitation is attributed to seasonal variations, variability in sea ice extent, and supersaturation of vapor over ice at low temperatures (Risi et al. 2013; Schoenemann et al. 2014).

Supersaturation of vapor over ice. In order to interpret polar precipitation records, one needs to account for the supersaturation effect at cloud temperatures <–20 °C (Jouzel and Merlivat 1984; Angert et al. 2004). The effect considers diffusive fractionation that occurs due to supersaturation of vapor over ice during precipitate formation which reduces the effective fractionation:

$$ {}^{*}\alpha_{\mathrm{eff}} = {}^{*}\alpha_{\mathrm{S\text{-}V\_eq}} \cdot {}^{*}\alpha_{\mathrm{kin}} \tag{14} $$

where ${}^{*}\alpha_{\mathrm{kin}}$ is the kinetic fractionation factor for vapor supersaturation over ice and given by (Jouzel and Merlivat 1984; Angert et al. 2004):

$$ {}^{*}\alpha_{\mathrm{kin}} = \frac{S}{{}^{*}\alpha_{\mathrm{S\text{-}V\_eq}} \cdot {}^{*}\alpha_{\mathrm{diff}} \cdot (S-1)+1} \tag{15} $$

The supersaturation coefficient (*S*) determines the relative contribution of diffusive and equilibrium fractionation during ice formation from vapor. *S* is dimensionless and a linear function of temperature, *T* (in °C), and the site-specifically adjusted factor *m* (Jouzel and Merlivat 1984):

$$ S = 1 - m \cdot T \tag{16} $$

Typical values for *m* in polar regions range from 0.001 to 0.008 (e.g., Masson-Delmotte et al. 2005; Steen-Larsen et al. 2011; Landais et al. 2012a, b). Higher *m* values (and thus higher *S*) increase the diffusive contribution, resulting in a steeper $\lambda^{17}_{\mathrm{GMWL}}$ as it is observed in low δ^{18}O snow (Fig. 3). $m=0$ (or $S=1$) will accordingly result in pure equilibrium fractionation. Even though Arctic precipitation shows positive ^{17}O-excess with respect to

continental Antarctic precipitation, supersaturation of vapor over ice is also identified as a driving mechanism for ^{17}O-excess at the NEEM drilling site, Greenland (Landais et al. 2012b). On the other hand, elevated supersaturation leads to lower λ^{2}_{GMWL} (d-excess) in polar precipitation. This is explained by a much lower δD-δ^{18}O slope of solid–vapor fractionation at low temperatures compared to the average equilibrium value of ≈ 8 (Landais et al. 2012a).

^{17}O-excess during strong evaporation in arid environments. Since evaporation results in a positive ^{17}O-excess in the vapor phase, residual water that experiences evaporation is left with a negative ^{17}O-excess with respect to the initial water (Fig. 4). Based on the Craig and Gordon Model and Equation (6), the isotopic evolution of an evaporating water body can be predicted as a function of h and $^{*}R_A$. Two general pathways of evaporating water bodies can be distinguished (Fig. 5), based on their hydrological setting that either excludes (Eqns. 17 to 19) or includes (Eqns. 20 and 21) groundwater recharge.

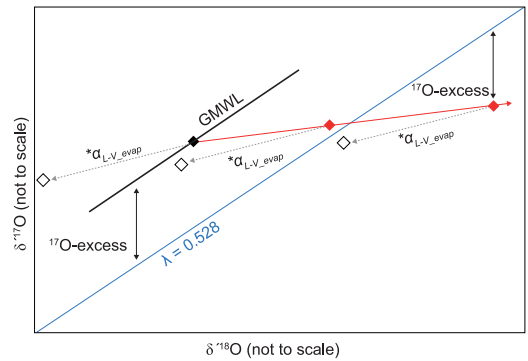

Figure 4. Fractionation of triple oxygen isotopes in an evaporating water body. The initial water body (**black diamond**) evolves along the **red trend** after experiencing evaporation. The resulting trajectory is flatter than the reference slope (**blue**), causing a negative ^{17}O-excess in the residual water (**red diamonds**) with respect to the initial water. Secondary vapor (**white diamonds**) which is formed by continental evaporation has a positive ^{17}O-excess with respect to the liquid phase.

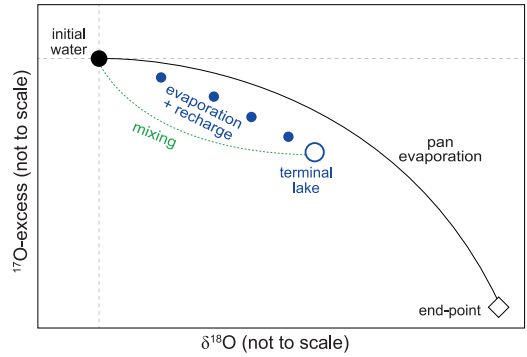

Figure 5. Schematics of oxygen isotope distribution during evaporation of a continental water body in different hydrological settings (modified from Surma et al. 2018). Simple (pan) evaporation (**solid black line**) follows a distinct evaporation trajectory towards the isotopic end-point ($^{*}R_{SS}$, **diamond**).$^{*}R_{SS}$ is balanced by the evaporative isotope flux and equilibrium exchange (Criss 1999). The value of $^{*}R_{SS}$ is determined by $^{*}R_A$ and h (see Eqn. 18). If the water body is additionally balanced by groundwater recharge, its isotopic composition will assume a steady state that falls below the pan evaporation trend (**solid blue circles**), depending on the *E/I* value. Increasing *E/I* leads to higher δ^{18}O and lower ^{17}O-excess—up to *E/I* = 1 (i.e. a stable terminal lake; **open blue circle**). Non-steady state admixture of initial water results in mixing lines (**dotted green line**) below evaporation trends, see also Voigt et al. (2020).

If the boundary parameters (${}^{*}R_{A}$, wind turbulence, isotopic composition of initial water) are well constrained, the isotopic compositions of water bodies in a non-recharged lake system (${}^{*}R_{W}$) provide information on average annual h of an arid region (Surma et al. 2015). The isotopic composition of a non-recharged water body (${}^{*}R_{W}$) is calculated by (Criss 1999):

$$ {}^{*}R_{W} = f_{\text{res}}^{u} \cdot \left({}^{*}R_{\text{WI}} - {}^{*}R_{\text{SS}} \right) + {}^{*}R_{\text{SS}} \tag{17} $$

where ${}^{*}R_{\text{WL}}$ is the isotopic composition of the initial water and ${}^{*}R_{\text{SS}}$ is the isotopic stationary state (end-point) which is dictated by ${}^{*}R_{\text{A}}$ and h:

$$ {}^{*}R_{\text{SS}} = \frac{{}^{*}\alpha_{\text{L-V\_eq}} \cdot h \cdot {}^{*}R_{\text{A}}}{1 - {}^{*}\alpha^{0}_{\text{L-V\_evap}} \cdot (1-h)} \tag{18} $$

The exponent u describes the liquid–vapor fractionation factor as a function of h:

$$ u = \frac{1 - {}^{*}\alpha^{0}_{\text{L-V\_evap}} \cdot (1-h)}{{}^{*}\alpha^{0}_{\text{L-V\_evap}} \cdot (1-h)} \tag{19} $$

where ${}^{*}\alpha^{0}_{\text{L-V\_evap}}$ is the total fractionation factor at a hypothetical relative humidity of $h = 0$. For $h = 0$ Equation (7) reduces to: ${}^{*}\alpha^{0}_{\text{L-V\_evap}} = {}^{*}\alpha_{\text{L-V\_eq}} \cdot {}^{*}\alpha_{\text{diff}}$. The isotopic composition of a water body in steady state (${}^{*}R_{\text{WS}}$) is calculated as a function of evaporation over inflow (E/I) by (Criss 1999):

$$ {}^{*}R_{\text{WS}} = \frac{{}^{*}\alpha^{0}_{\text{L-V\_evap}} \cdot (1-h) \cdot {}^{*}R_{\text{WI}} + {}^{*}\alpha_{\text{L-V\_eq}} \cdot h \cdot E/I \cdot {}^{*}R_{\text{A}}}{E/I + {}^{*}\alpha^{0}_{\text{L-V\_evap}} \cdot (1-h) \cdot (1 - E/I)} \tag{20} $$

In the case of a terminal lake setting ($E/I = 1$), Equation (20) reduces to:

$$ {}^{*}R_{\text{WS}} = {}^{*}\alpha^{0}_{\text{L-V\_evap}} \cdot (1-h) \cdot {}^{*}R_{\text{WI}} + {}^{*}\alpha_{\text{L-V\_eq}} \cdot h \cdot E/I \cdot {}^{*}R_{\text{A}} \tag{21} $$

A case study on saline ponds in the hyper-arid Atacama Desert demonstrates that isotopic compositions of recharged water bodies (${}^{*}R_{\text{WS}}$) can be accurately modeled for given boundary conditions. If h and ${}^{*}R_{\text{A}}$ are monitored independently, ^{17}O-excess—in combination with d-excess—is a useful tracer for the assessment of lake balances and h and parametrization of wind effects (Surma et al. 2018). A recent study shows, that unlike in classic δD and δ^{18}O isotope hydrology, δ^{17}O allows for the separation of mixing and evaporation (Voigt et al. 2020).

Triple oxygen isotopes in rainfall and mid-latitude snow. Li et al. (2015) show a strong latitude effect in ^{17}O-excess in tap waters across the US. The samples reflect the integrated average isotopic composition of regional precipitation. Lowest ^{17}O-excess values were found around the Gulf of Mexico (–6 to 12 per meg), whereas highest values were found in Northwestern U.S. (31 to 43 per meg). In general, these variations are mainly a product of rain amount effects, re-evaporation of meteoric water, and mixing with groundwater. Humidity conditions at precipitation moisture sources do not explain the observed variability, therefore the authors stress that local, continental moisture recycling may indeed be responsible for elevated ^{17}O-excess in precipitation, as discussed by other authors (Landais et al. 2010; Li et al. 2015; Tian et al. 2019). Bershaw et al. (2020) also observe slightly elevated ^{17}O-excess in surface waters from Northwestern U.S. and suggest an effect of analytical uncertainty and/or the admixture of stratospheric vapor as a potential mechanism (the role of stratospheric intrusions in mid-latitudes is discussed in the following section). Tap waters in the Central U.S. deviate from the latitudinal gradient and show anomalously low values which are linked to different moisture sources. This is also confirmed by higher resolution precipitation records for the region, even though subcloud re-evaporation

of rainfall in spring and summer is also identified as a seasonal controlling mechanism for ^{17}O-excess (Tian et al. 2018). This is shown by a large range of ^{17}O-excess (–17 to 64 per meg) and a flatter slope of the local meteoric water line (λ^{17}_{LMWL}) compared to λ^{17}_{GMWL}. Landais et al. (2010) show that subcloud re-evaporation of rainfall during African monsoon in tropical Niger may alter ^{17}O-excess in precipitation by ~40 per meg over the course of a single rain event. Highest values are found in samples that precipitated at the beginning of the event, whereas precipitate that was formed at the end shows a more negative ^{17}O-excess. This shift is linked to the decrease in relative humidity over the course of the rain event.

A two-year precipitation record on the maritime island of Okinawa, Japan, reveals that ^{17}O-excess of local rainfall varies with seasonal change of air mass trajectories. Thus, ^{17}O-excess in coastal regions is largely controlled by variable humidity conditions at different source regions (Uechi and Uemura 2019). The authors also discuss that careful selection of a representative reference line (e.g., $\lambda^{17} = 0.527$ instead of 0.528) may avoid artificially inflated ^{17}O-excess values which is also subject of discussion for the trend observed at Alert, Canada (Lin et al. 2013a,b; Miller 2013).

Precipitation data from Indiana, U.S., show that local precipitation is in general agreement with λ^{17}_{GMWL} (Tian et al. 2018). However, the authors observe notably lower $\lambda^{17}_{LMWL} = 0.5258$ for precipitation sampled in summer which hat lower average ^{17}O-excess compared to winter precipitation and is associated with re-evaporation. The corresponding δD vs. δ^{18}O slopes (λ^{2}_{LMWL}) are slightly lower than λ^{2}_{GMWL}. A comparable λ^{17}_{LMWL} (= 0.5264) was found in summer precipitation samples from NW China. Since these samples were associated with relatively high ^{17}O-excess, the authors suggest a contribution from re-evaporated earlier rainfall events (Tian et al. 2019).

Isotope values of snow from Mt. Zugspitze (this work) range from –21.7 to –8.3‰ in $\delta^{18}O_P$, from 17 to 62 per meg in ^{17}O-excess$_P$, and from 4 to 16‰ in d-excess$_P$ (Figs. 3 and 6). A slightly negative correlation of ^{17}O-excess$_P$ with $\delta^{18}O_P$ of $\lambda^{17}_{LMWL} = 0.5272 \pm 0.0006$ is observed indicating a somewhat steeper ^{17}O-excess-δ^{18}O relation than the GMWL (Fig. 6). The local λ^{2}_{LMWL} of 8.1 ± 0.3 is in good agreement with global average and also with local precipitation records reported for the Zugspitze plateau (λ^{2}_{LMWL} = 7.95; Hürkamp et al. (2019)) and for Garmisch-Partenkirchen ($\lambda^{2}_{LMWL} = 8.12$; Stumpp et al. (2014)). The range of isotope distribution in snow cover of the Zugspitze plateau is also consistent with the isotope distribution in collected snowfall (cf. Tables S3 and S7). Affolter et al. (2015) report comparable $\lambda^{17}_{LMWL} = 0.527$ and $\lambda^{2}_{LMWL} = 7.92$ for precipitation collected across Switzerland.

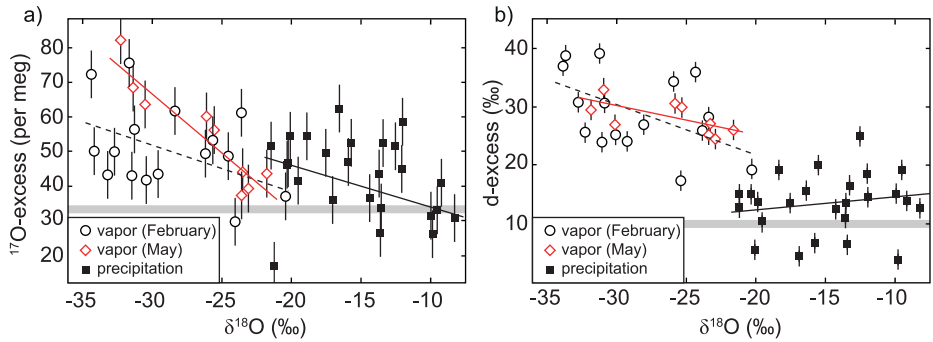

Figure 6. Isotope data of vapor from February (open circles) and May (open diamonds), and freshly precipitated snow (solid squares) from Mt. Zugspitze. Gray lines represent the GMWL, dashed, red, and solid black lines represent λ^{17} and λ^{2} of vapor in February and May and in total precipitation, respectively. λ^{17}_{A} and λ^{2}_{A} of vapor data are generally flatter than the GMWL, resulting in a decrease of ^{17}O-excess$_A$) and d-excess$_A$ ($\lambda^{2}_{A\_Feb} = 7.3 \pm 0.4$, $\lambda^{2}_{A\_May} = 7.5 \pm 0.2$) with increasing $\delta^{18}O_A$ (also see Table S5). This lower slope is also visible in ^{17}O-excess$_P$ of precipitation ($\lambda^{17}_{P} = 0.5272 \pm 0.0006$, $\lambda^{17}_{P} = 0.5272 \pm 0.0006$) but not in respective d-excess$_P$ ($\lambda^{2}_{P} = 8.1 \pm 0.3$). See Tables S6 and S7 for data.

^{17}O-EXCESS DISTRIBUTION IN ATMOSPHERIC VAPOR

Only a few studies investigated the triple oxygen isotope composition of atmospheric vapor so far. Figure 7 shows a compilation of isotope data from samples collected above the Pacific Ocean, the NEEM drilling site, Greenland, in Alert, Canada, and at Mt. Zugspitze, Germany (Uemura et al. 2010; Landais et al. 2012b; Lin et al. 2013; this study).

Lowest ^{17}O-excess values (–6 to 46 per meg) are associated with most positive δ^{18}O values in the range of –23 to –11‰ in primary atmospheric vapor above the Pacific Ocean's surface (Uemura et al. 2010). A negative correlation of ^{17}O-excess with relative humidity was identified (–0.64 per meg/%). Assuming closure for vapor above the open ocean, the authors built on the Craig and Gordon Model and the relationship of ^{17}O-excess vs. relative humidity (h) as described by (Barkan and Luz 2007):

$$^{17}\text{O-excess} = -\ln\left\{{}^{17}\alpha_{\text{L-V\_eq}} \cdot \left({}^{17}\alpha_{\text{diff}} \cdot (1-h) + h\right\}\right. \\ +0.528 \cdot \ln\left\{{}^{18}\alpha_{\text{L-V}_{\text{eq}}} \cdot \left({}^{18}\alpha_{\text{diff}} \cdot (1-h) + h\right\}\right. \quad (22)$$

In order to fit the output of Equation (22) to actual measurement data, Uemura et al. (2010) found the correction exponent for boundary layer turbulence (Eqn. 9) to be $n = 0.29$ ($^{18}\alpha_{\text{diff(corr)}} = 1.008$) above the open sea which is somewhat higher than a previously reported correction by Merlivat and Jouzel (1979) that was based on wind tunnel experiments ($n = 0.18$, $^{18}\alpha_{\text{diff(corr)}} = 1.005$). Luz and Barkan (2010) recalculated the correction by Uemura et al. (2010) for a seawater value with ^{17}O-excess of –5 per meg, yielding $n = 0.33$ ($^{18}\alpha_{\text{diff(corr)}} = 1.0092$). This relation provides a basis to quantify h based on ^{17}O-excess variations in remote vapor and precipitation. Landais et al. (2012b) show that ^{17}O-excess in vapor (15 to 48 per meg) at the NEEM drilling site in Greenland varies in the same range as ^{17}O-excess in contemporaneous precipitation (23 to 43 per meg). This observation confirms that triple oxygen isotopes in polar snow reflect the composition of atmospheric vapor when $\theta_{\text{S–V\_eq}} = 0.528$ is applied.

The highest values and largest variations of ^{17}O-excess (23 to 190 per meg) in a single study were reported for vapor samples from Alert, in arctic Canada (Lin et al. 2013a). The positive anomalies were explained with stratospheric intrusions that contain mass-independent oxygen isotope signatures, but this interpretation was not independently verified.

Atmospheric vapor samples from Mt. Zugspitze (Figs. 6 and 7) show elevated ^{17}O-excess between 30 and 82 per meg with decreasing δ^{18}O (–34.4 to –20.4‰) and a δ'^{17}O–δ'^{18}O trend of $\lambda_A^{17} = 0.5265 \pm 0.0006$. A difference is observed between vapor that was sampled in February ($\lambda_A^{17} = 0.5270 \pm 0.0007$) and vapor that was sampled in May (λ_A^{17} of 0.5245 ± 0.0005), the latter showing a clearer correlation of ^{17}O-excess with δ^{18}O (Fig. 6 a). Corresponding δD_A vs. $\delta^{18}O_A$ (λ_A^2) for February and May are nearly identical within error (Fig. 6 b). In general, all slopes are somewhat flatter than the GMWL ($\lambda_{\text{GMWL}}^{17} = 0.528$, $\lambda_{\text{GMWL}}^2 = 8$; Dansgaard 1964; Luz and Barkan 2010). The average isotopic composition of vapor is shifted by $\Delta\delta^{18}O_{A–P} = -12.9$‰, $\Delta^{17}\text{O-excess}_{A\text{-}P} = 10$ per meg, and $\Delta\text{d-excess}_{A\text{-}P} = 18$‰ with respect to the average isotopic composition of local precipitation (Figs. 6 and 8). Regression analysis demonstrates, that local variations in ${}^*R_A$ (and also ${}^*R_P$) are largely unrelated to meteorological conditions (T_a, h), except for $\delta^{18}O_A$, which is positively correlated with T_a (Table 1).

Even though the regular occurrence of deep stratospheric intrusions is also evident at Mt. Zugspitze (Trickl et al. 2010), we may probably exclude a mass-independent signal in ^{17}O-excess of ambient vapor, since vapor concentrations in stratospheric air are extremely low. High positive ^{17}O anomalies (1000 to 1800 per meg) were observed in the in the southern high-latitude stratosphere at vapor concentrations below 10 ppm and more than 1 km above the tropopause (Franz and Röckmann 2005). Therefore, exceptionally dry air in the lower troposphere would be

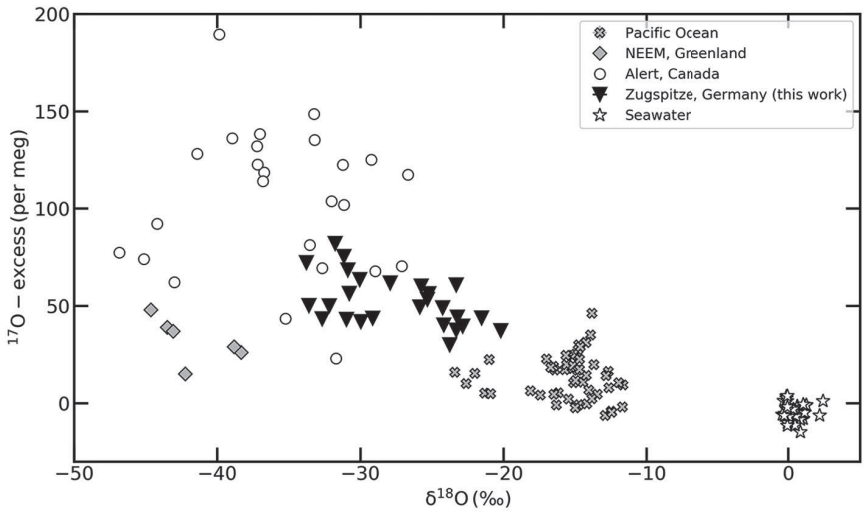

Figure 7. Compilation of ^{17}O-excess vs. δ^{18}O in atmospheric vapor samples and seawater (**asterisks**). Atmospheric vapor that was sampled above the Pacific Ocean (**crosses**) shows most positive δ^{18}O values and covers the lower range in ^{17}O-excess from −6 to 46 per meg (Uemura et al. 2010). Variations are attributed to variable *h* above the evaporating sea surface. Vapor samples from Alert, Canada (**open circles**) show the largest range and highest absolute values in ^{17}O-excess (Lin et al. 2013a). However, data consistency of that study has been questioned (Lin et al. 2013b; Miller 2013). Atmospheric vapor that was samples at the NEEM drilling site, Greenland (**diamonds**), range from −45 to −38‰ in δ^{18}O and from 20 to 50 per meg in ^{17}O-excess (Landais et al. 2012b). Samples were found to be in equilibrium with local precipitation and in good agreement with a Rayleigh condensation model, also reflecting moisture source conditions. Ambient vapor samples from Mt. Zugspitze, Germany (**triangles**), range from −34 to −20‰ in δ^{18}O and from 30 to 80 per meg in ^{17}O-excess, indicating a negative correlation of ^{17}O-excess with δ^{18}O (this study).

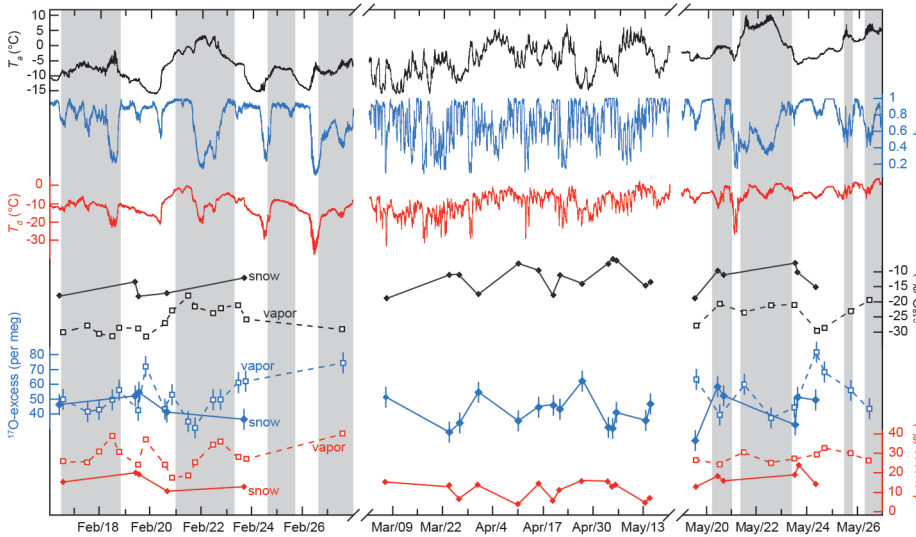

Figure 8. Record of Schneefernerhaus Research Station meteorological data: 2 m air temperature (T_a), relative humidity (*h*), and dew point temperature (T_d) from 2016–02–16 to 2016–05–27. Isotope data (δ^{18}O, ^{17}O-excess, and d-excess) are shown for atmospheric vapor (**open symbols, dashed lines**) and precipitation (**solid symbols and lines**). Gray sequences indicate warmer periods. Note the scale contraction for the period between 2016–02–28 and 2016–05–19. Error bars are ±1σ SE for ^{17}O-excess and d-excess, and smaller than symbol size for δ^{18}O. Meteorological data for time of sample collection is provided in Tables S1 and S2 in the Supporting Information.

necessary in order to achieve low mixing ratios of tropospheric vapor and, thus, a conservation of the stratospheric signal in the mass balance: i) vapor concentrations at Mt. Zugspitze did not fall below 2000 ppmv during vapor extractions, so that photochemically induced anomalies are unlikely to be evident in our samples (Hausmann et al. 2017). A mass-balance calculation with local vapor ($\delta^{18}O = -22.8‰$, ^{17}O-excess = 40 per meg 2000 ppmv vapor concentration) and hypothetical stratospheric vapor ($\delta^{18}O = -64.1‰$, ^{17}O-excess = 1300 per meg, 7.3 ppmv concentration; average values obtained from high ^{17}O-excess samples reported by Franz and Röckmann 2005) would yield a mix with $\delta^{18}O = -23.2$ and ^{17}O-excess = 43 per meg. ii) The mid-latitude tropopause is considerably higher (7–10 km) compared to polar regions (~6 km), limiting the contribution of stratospheric downdrafts to the lower troposphere. Nevertheless, more data of ambient vapor and would hold the potential to prove the effect of stratospheric deep intrusions on the oxygen isotope balance. The event of highest ozone of 101.9 ppbv registered at Zugspitze (Hausmann et al. 2017) is 50 ppbv in excess above the tropospheric ozone background of ~50 ppbv. In comparison, old stratospheric air in polar vortex contains at ~3 to 4 ppmv ozone (e.g., El Amraoui et al. 2018) which is >3000 ppbv above tropospheric ozone background. Therefore, the isotopic balance of atmospheric vapor at mid-latitudes is likely dominated by synoptic processes (i.e., Rayleigh distillation and potential continental recycling).

Rayleigh distillation. Several studies have demonstrated that ^{17}O-excess in vapor and precipitation reflects evaporation conditions at the initial moisture source (Uemura et al. 2010; Landais et al. 2012b; Uechi and Uemura 2019). However, as summarized above in the discussion of mid-latitude rainfall data, there is some indication of subsequent modification by evaporative recycling of continental moisture. With the Mt. Zugspitze data at hand, we may test the respective primary and subsequent controls of water vapor isotopic composition. ${}^{*}R_A$ in the troposphere at high altitude and—by inference—the continental interior. Rozanski et al. (1982) have demonstrated that formation of condensate from vapor in westerly air masses may be well approximated by a Rayleigh approach. δD_A and d-excess$_A$ analyses by Dütsch et al. (2018) demonstrate that the occurrence of mixed phase clouds is negligible for westerly moisture pathways, thus, excluding complexity of vapor, water, and ice coexistence during cloud formation (Ciais and Jouzel 1994). This is also supported by the liquid–vapor precipitate formation in rapidly advected air masses at Mt. Zugspitze. Based on the analysis of 11 snow and vapor samples that were collected simultaneously (Table S2, Roman numerals), we determined to overlying fractionation process for snow formation at Mt. Zugspitze. Observed deviation of actual samples ($^{18}\varepsilon_{A\text{–}P\_meas}$ from predicted fractionation ($^{18}\varepsilon_{A\text{–}P\_cal}$) is calculated by $\Delta^{18}\varepsilon_{A\text{–}P}$ ($^{18}\varepsilon_{A\text{–}P\_meas} - {}^{18}\varepsilon_{A\text{–}P\_cal}$), with $^{18}\varepsilon_{A\text{–}P\_meas} \approx {}^{18}O_p - {}^{18}O_A$ and:

$$^{18}\varepsilon_{A\text{-}P\_cal} = (^{18}\varepsilon_{S\text{-}V\_eq} - 1) \cdot 1000 \quad (23)$$

where $^{18}\alpha_{S\text{–}V\_eq}$ is the solid–vapor equilibrium fractionation factor (Majoube 1971). $\Delta^{18}\varepsilon_{A\text{–}P}$ based on this calculation averages $-4.4 \pm 2.0‰$ (Fig. 9). Replacing $^{18}\alpha_{S\text{–}V\_eq}$ in Equation (23) with $^{18}\alpha_{L\text{–}V\_eq}$ to account for the occurrence of supercooled water droplets provides a better approximation for $^{18}\varepsilon_{A\text{–}P\_meas}$ ($\Delta^{18}\varepsilon_{A\text{–}P} = 1.9 \pm 0.9‰$) (Ciais and Jouzel 1994; Bolot et al. 2013), thus confirming that liquid orographic clouds are the prevalent cloud species in strong updraft regimes at temperatures between 0 and −15 °C, such as Mt. Zugspitze (Kneifel et al. 2014; Lohmann et al. 2016; Lowenthal et al. 2016). Respective ^{17}O-excess$_{P_cal}$ and d-excess$_{P_cal}$ deviate by 19 ± 19 per meg and $11.1 \pm 4.3‰$. Due to their large scatter, these values are also reasonably well reproduced at given uncertainty, even though d-excess$_P$ is systematically lower, presumably due to the different T dependencies of $^{2}\alpha_{L\text{–}V\_eq}$ and $^{18}\alpha_{L\text{–}V\_eq}$. Typically, the orographic cloud basis is located either below or at the altitude of Mt. Zugspitze, hence we assume that pairs of vapor–precipitation samples are closely related. However, vapor samples may potentially not represent free atmospheric vapor but a mixture of atmospheric and snow surface vapor. We also note that the determination of ${}^{*}\alpha_{L\text{–}V\_eq}$ does not cover T below 0 °C and is therefore extrapolated for ambient conditions at Mt. Zugspitze (Horita and Wesolowski 1994).

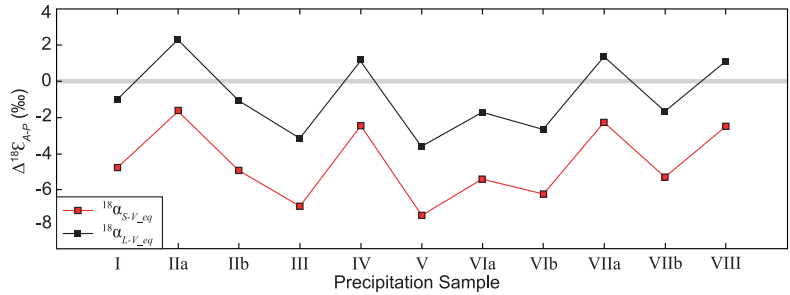

Figure 9. Difference between measurement data of precipitation samples and predicted isotopic composition of precipitation ($\Delta^{18}\varepsilon_{A\text{–}P}$). Values are calculated with $^{18}\alpha_{L\text{–}V\_eq}$ (**solid black squares and line**, Horita and Wesolowski 1994) and $^{18}\alpha_{S\text{–}V\_eq}$ (**solid red squares and line**, Majoube 1971).

The evolution of $^{*}R_A$ (Fig. 10) is based on Monte Carlo simulations (n=500) for Equations (11) and (13), using a $^{*}R_{W_0}$ of ocean surface with δD_{W_0}=0‰, $\delta^{17}O_{W_0}$= –0.005‰, and $\delta^{18}O_{W_0}$=0‰. Modeling parameters (source h, T_a, $^{*}\alpha_{diff}$, $^{*}\alpha_{L\text{–}V\_eq}$) were approximated from HYSPLIT air trajectory reanalysis (see Table S8 for details). $^{*}\alpha_{diff}$ is corrected for air turbulence by Equation (9) with an average n=0.26 (Merlivat and Jouzel 1979; Luz and Barkan 2010). The range of observed $\delta^{18}O_A$ is well reproduced for f_{res} between 0.5 (days of relatively warm T_a) and 0.15 (days of lower T_a). Higher $\delta^{18}O_A$ is found in vapor from warmer air masses and lower $\delta^{18}O_A$ in vapor provided by cold air (Fig. 8), indicating a distillation effect that is also in agreement with the HYSPLIT output for specific humidity. This observation is also confirmed by regression analysis of $\delta^{18}O_A$ vs. T_a (Table 1). A change from a warmer (25 °C) to a cooler (10 °C) vapor source would shift $\delta^{18}O_A$ according to the change in equilibrium fractionation during vapor formation (Fig. 10, blue arrows), which is only a minor effect compared to that of relative condensation loss from the air parcel. The variability in $^{17}O\text{-excess}_A$ is controlled by ambient h and wind turbulence (n) at the moisture source (e.g., Uemura et al. (2010); Uechi and Uemura (2019)). The magnitude of initial $d\text{-excess}_A$ is, in contrast, additionally controlled by surface temperature at the source, resulting from the different T dependency of $^{2}\alpha_{L\text{–}V\_eq}$

Table 1. Regression analysis (slope, standard error (*SE*), and coefficient of determination (R^2) of $\delta^{18}O$, ^{17}O-excess, and d-excess in vapor and precipitation samples vs. meteorological parameters (left column): Air temperature (T_a) and relative humidity (h).

Parameter	**$\delta^{18}O$**			**^{17}O-excess**			**d-excess**		
	slope	SE	R^2	slope	SE	R^2	slope	SE	R^2
				Vapor (total)					
T_a	0.52	0.11	0.47	–0.81	0.48	0.11	–0.01	0.20	0.00
h	–1.46	4.36	0.00	14.53	13.79	0.05	–12.14	4.82	0.22
				Vapor (February)					
T_a	0.70	0.18	0.51	–1.50	0.70	0.25	0.05	0.40	0.00
h	5.27	5.31	0.07	2.66	5.31	0.00	–20.80	6.17	0.45
				Vapor (May)					
T_a	0.51	0.24	0.40	–1.78	0.98	0.32	–0.04	0.19	0.01
h	–12.49	5.90	0.39	44.65	24.06	0.33	4.36	4.33	0.13
				Precipitation (total)					
T_a	0.21	0.17	0.06	0.03	0.50	0.00	–0.51	0.31	0.18
h	4.70	5.69	0.03	–27.08	15.23	0.12	–12.26	11.02	0.09

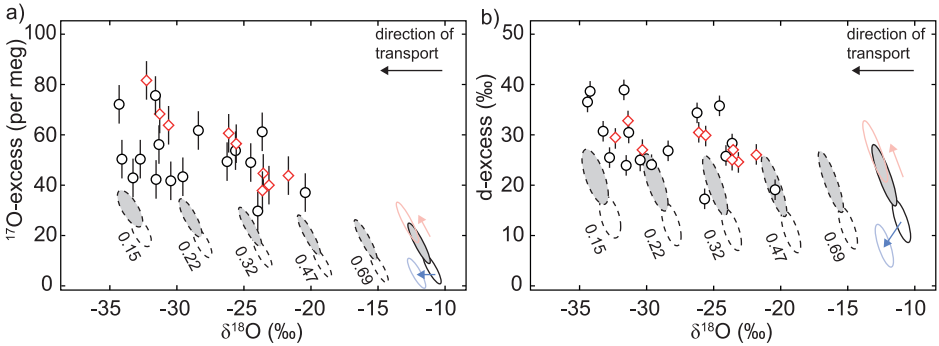

Figure 10. Rayleigh fractionation model for initial atmospheric vapor at given source condition for ^{17}O-excess$_A$ vs. $\delta^{18}O_A$ **(a)**, and for d-excess$_A$ vs. $\delta^{18}O_A$ **(b)**. Simple Rayleigh distillation of initial oceanic vapor (**solid frame**, $f_{res}=1$) at $h_s=0.8$ (**white**) and at $h_s=0.6$ (**gray**) results in steady isotopic depletion of $^{*}R_A$. Numbers represent respective f_{res}. **Blue arrows** indicate a change in T_s from 25 to 10 °C, **red arrows** the change if a wind correction exponent of $n=0.29$ instead of $n=0.23$ is used. **Ellipsoids** represent probability density functions for a 0.95 quantile of the Monte Carlo simulation. **Black and red open symbols** represent atmospheric vapor sampled in February and May at Mt. Zugspitze, respectively.

and $^{18}\alpha_{L\text{–}V\_eq}$, and $\frac{^{2}\alpha_{diff}}{^{18}\alpha_{diff}}$ (Horita and Wesolowski 1994; Luz et al. 2009). Although the range of $\delta^{18}O_A$ may be successfully modeled by continuous vapor distillation to a reasonable degree, high ^{17}O-excess$_A$ and d-excess$_A$ values are not reproduced. Variation of from $n=0.26$ to $n=0.33$ do not sufficiently increase ^{17}O-excess$_A$ and d-excess$_A$ values (Fig. 10, red arrows). Lower h over the ocean might also elevate initial ^{17}O-excess$_A$ and d-excess$_A$, but $h < 0.6$ is unlikely for given oceanic moisture sources (Pfahl and Sodemann 2014). Consequently, Rayleigh distillation alone may not explain the observation.

Moisture pathways and air trajectory modeling. Reanalysis of air trajectories provides important information on atmospheric pathways and potential moisture sources (Pfahl and Wernli 2008; Vogelmann et al. 2015; Yu et al. 2015; Uechi and Uemura 2019). Atmospheric transport to Mt. Zugspitze is determined by three patterns: (i) Long-range transport from North America, (ii) long-range transport from Northern Africa, and (iii) stratospheric deep intrusions (Hausmann et al. 2017). We modeled 240 h back-trajectories (including T_a and specific humidity) using the NOAA HYSPLIT software package and GDAS reanalysis data sets (available at ftp://arlftp.arlhq.noaa.gov/pub/archives/gdas1) (Stein et al. 2015). Since the higher resolution record (0.5° grid) is incomplete, we use datasets of 1.0° spatial resolution for modeling. According to previous studies we use altitudes of 1,900 to 2,200 m above ground level (m a.g.l.) to approximate the low-level troposphere (3,000 m a.s.l.) at Mt. Zugspitze (Trickl et al. 2010; Vogelmann et al. 2015) and identify two source patterns: The Central Atlantic, between N 30° and N 50° for warmer air, and the Nordic Sea providing cold air (Fig. 11). These patterns are also in agreement with general moisture pathways that were determined for the Northern Alps by Sodemann and Zubler (2010). Analysis of specific humidity indicates low continental evaporation rates in winter with the Central Atlantic being identified as the predominant moisture source in February, whereas moisture uptake above Western and Central Europe contributes to the moisture balance in late spring.

Continental moisture recycling. Triple oxygen isotope studies of mid-latitude waters suggest that continental recycling may be an important local effect (Li et al. 2015; Tian et al. 2018; Tian et al. 2019) but a rigorous demonstration has not been provided yet. It is also known from δD and $\delta^{18}O$ analyses that moisture recycling plays an important role in the continental moisture balance (Bastrikov et al. 2014; Wei and Lee 2019). The continental vapor budget ($^{*}R_A$) is therefore balanced by the isotopic composition of initial vapor ($^{*}R_{A_0}$) and the surface vapor flux ($^{*}R_V$) with q_R being the relative quantity of local, recycled moisture (Aemisegger et al. 2014):

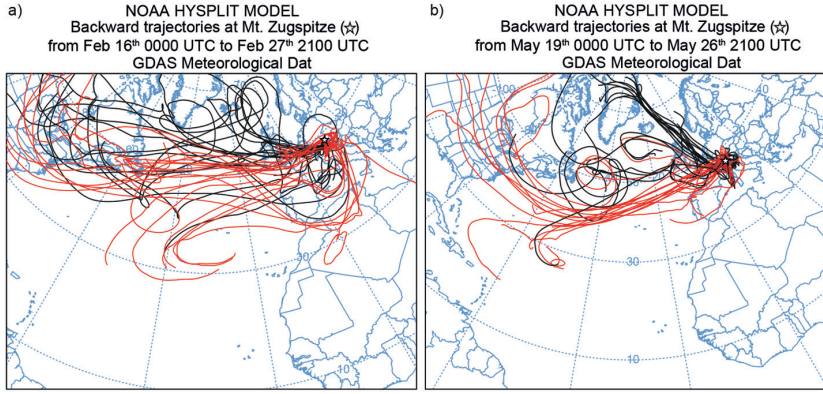

Figure 11. HYSPLIT 240 h back trajectories (modelled for 2,200 m a.g.l. and 3 h resolution) of air masses arriving at Mt. Zugspitze (**asterisk**). Modeling is performed for both field campaigns in February **(a)** and May **(b).** Trajectories of warmer air masses (**red**) suggest moisture uptake above the Central Atlantic Ocean, colder air masses (**black**) cross the Northern Atlantic and the Nordic Sea.

$$ {}^{*}R_{\mathrm{A}} = \left(1-q_{\mathrm{R}}\right)\cdot {}^{*}R_{\mathrm{A}_0} + q_{\mathrm{R}}\cdot {}^{*}R_{\mathrm{V}} \tag{24} $$

The surface vapor flux is defined as:

$$ {}^{*}R_{\mathrm{V}} = q_{\mathrm{T}}\cdot {}^{*}R_{\mathrm{V_T}} + \left(1-q_{\mathrm{T}}\right)\cdot {}^{*}R_{\mathrm{V_E}} \tag{25} $$

where q_{R} is the relative quantity of recycled vapor being contributed by plant transpiration and ${}^{*}R_{\mathrm{V_T}}$ the corresponding isotopic ratio which is approximated by quantitative, non-fractionating transfer from surface water (${}^{*}R_{\mathrm{W}}$) to vapor, so that ${}^{*}R_{\mathrm{V_T}}={}^{*}R_{\mathrm{W}}$ (Wang and Yakir 2000; Peng et al. 2005). It has been shown that moisture of the continental boundary layer is significantly balanced by recycling of surface water (He and Smith 1999; Welp et al. 2012; Jasechko et al. 2013). ${}^{*}R_{\mathrm{V_E}}$is the isotopic ratio of the evaporative flux from surface waters and saturated soil (${}^{*}R_{\mathrm{W_i}}$). Figure 12 outlines the process of initial vapor formation and continental recycling.

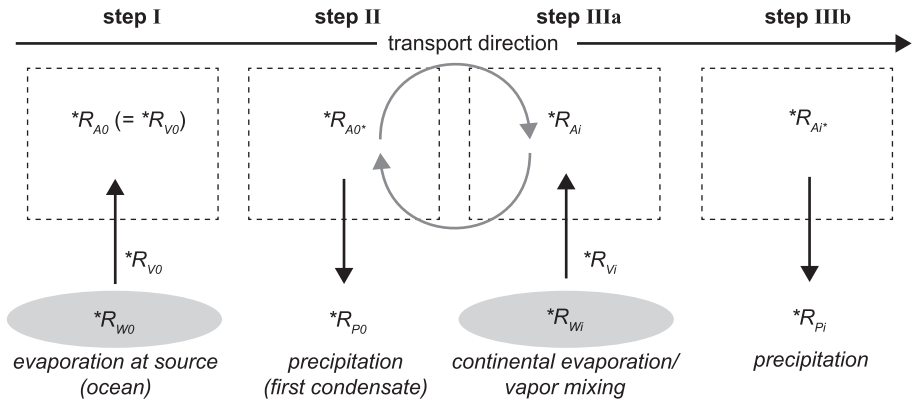

Figure 12. Schematic representation showing isotopic fluxes during Rayleigh distillation with continental recycling: **I.** Initial vapor forms above the ocean surface. **II.** First condensate formation and precipitation. **III (a and b)**. Evaporation of continental surface water, admixture of vapor, and subsequent precipitation. Solid, **black arrows** indicate H_2O fluxes, **gray arrows** indicate mixing of residual vapor with secondary vapor.

The results from HYSPLIT air trajectory reanalysis (see above) and previous studies suggest that moisture recycling above Western and Central Europe affects the balance of ${}^{*}R_{A_0}$ (van der Ent et al. 2010; Sodemann and Zubler 2010). Based on the 1D-model (Fig. 12), we here use Equations (11), (13), (24), and (25) to calculate the evolution of atmospheric vapor, ${}^{*}R_{A_i}$ (Fig. 13 a and b). Average $q_T = 0.7$ is suggested by different previous studies for Central Europe (Lawrence et al. 2007; Aemisegger et al. 2014; Christner et al. 2017). Wind-induced turbulence (Eqn. 9) for continental evaporation is parametrized with $n = 0.5$ (Dongmann et al. 1974; Gat 1996; Haese et al. 2013). ${}^{*}R_{W_i}$ is approximated with mean regional ${}^{*}R_p$ (February: $\delta^{17}O \approx -5.525‰$, $\delta^{18}O \approx -10.5‰$, $\delta D \approx -74.0‰$; May: $\delta^{17}O \approx -4.199‰$, $\delta^{18}O \approx -8.0‰$, $\delta D \approx -54.0‰$), using average precipitation over Western to Central Europe from the *Online Isotopes in Precipitation Calculator* (OIPC) (Bowen and Revenaugh 2003; Bowen 2018) with ${}^{17}O$-excess being expected to be close to the average GMWL value (≈ 33 per meg).

Continental recycling shows a small increase of ${}^{17}O\text{-excess}_A$ for higher q_R (Fig. 13 a), whereas no significant effect is visible for d-excess_A (Fig. 13 b). Changing ${}^{*}R_W$ of surface water to lower values (February) results in an according shift in $\delta^{18}O_A$ which is visibly larger for $q_R = 0.5$ but does not affect both excess parameters. This may be explained by the fact that average surface water's $\text{d-excess}_W \approx 10‰$ and, thus, lower than d-excess_A of arriving moisture (≈ 10‰). Evaporation from surface water will elevate d-excess_V in the local vapor flux to a degree which is not significantly different from arriving d-excess_A. ${}^{17}O\text{-excess}_W$ in surface water, on the other hand, is already comparably high to ${}^{17}O\text{-excess}_A$ in the arriving air parcel. Re-evaporation elevates ${}^{17}O\text{-excess}_V$ in the vapor flux and induces a positive shift in the resulting mixed vapor. Since typical q_R is below 0.2 during winter and spring in Western and Central Europe, the uncertainty in ${}^{*}R_W$ may be neglected here (Trenberth 1999; van der Ent et al. 2010). However, an accurate estimate will be more critical when recycling is balanced for summer months and intensive evaporation elevates q_R and significantly alters ${}^{*}R_W$.

Vapor contribution from a local evaporation. Considering the above findings, recycling over continental Europe may probably explain some increase in ${}^{17}O\text{-excess}_A$ and should be accounted for in the total balance but is not sufficient to explain high ${}^{17}O\text{-excess}_A$ and d-excess_A found in atmospheric vapor at Mt. Zugspitze. Even at low continental $h = 0.6$ and $q_R = 0.5$—as used in this model—only a minor increase in ${}^{17}O\text{-excess}_A$ would result from this process. The effect on d-excess_A is even smaller. This is mainly due to the fact that transpiration by vegetation ($q_T = 0.7$) effectively diminishes fractionation of surface water during continental vapor formation. Much larger effects may be expected when vapor is formed from open water surfaces or saturated soil. However, the range of ${}^{17}O\text{-excess}_A$ modeled with low q_R is in good agreement with ${}^{17}O$-excess ranging from 14 to 27 per meg in natural water data reported for low altitudes in Western and Central Europe (Luz and Barkan 2010; Affolter et al. 2015; Alexandre et al. 2019). Our results also show that modeling with $q_R = 0.5$ provides sufficiently high ${}^{17}O$-excess (~40 per meg) to explain elevated values in precipitation as reported for Northwestern U.S. (Li et al. 2015) or inland China (Tian et al. 2019).

Even though the recycling ratio (q_R) is relatively small for Western and Central Europe at lower altitudes, evaporative loss from local snow cover provides significant vapor quantities in Alpine hydrological balances (Froehlich et al. 2008; van der Ent et al. 2010; Schlaepfer et al. 2014). Evaporation may account for up to 90% of total mass loss from snow cover and is especially high when turbulent transport of snow is effective, i.e., at wind-exposed locations and high-altitude mountain ridges (Strasser et al. 2008). Ambient conditions at Mt. Zugspitze are characterized by high snow accumulation and wind-induced re-deposition, providing a constant source of fresh snow surfaces, that i) lower a potential fractionation limitation by self-diffusion in stagnant snow cover (Friedman et al. 1991; Schlaepfer et al. 2014), and ii) can supply a significant quantity of moisture from local snow cover (Kaiser et al. 2002; Froehlich et al. 2008).

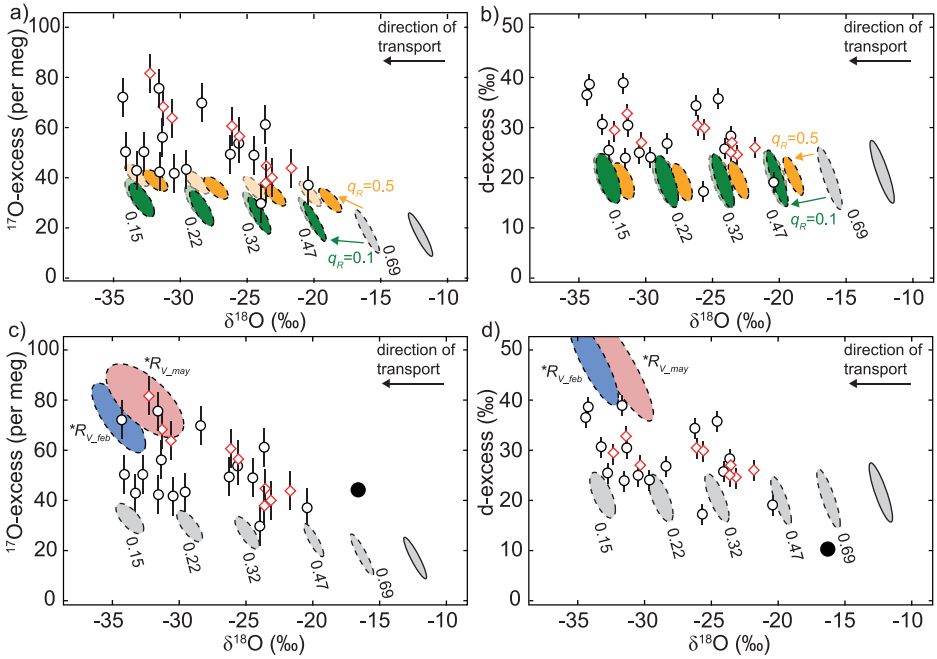

Figure 13. Distillation model as shown in Figure 10 but accounting for moisture recycling over Central Europe for ^{17}O-excess$_A$ vs. $\delta^{18}O_A$ **(a)**, and for d-excess$_A$ vs. $\delta^{18}O_A$ **(b).** Bold ellipsoids were modeled with average surface $^*R_W$ for May. Atmospheric vapor evolves along a Rayleigh condensation path (cf. Fig. 10) and mixes with hypothetical quantities of q_R=0.1 (**green**) and q_R=0.5 (**yellow**) of recycled moisture that evaporates from surface water ($^*R_W$). **Light ellipsoids** indicate same vapor trends but with average $^*R_W$ for February. Rayleigh fractionation model for atmospheric vapor including continental moisture recycling with q_R=0.2 at given f_{res} (**gray ellipsoids**, **numbers**) for for ^{17}O-excess$_A$ vs. $\delta^{18}O_A$ **(c)** and d-excess$_A$ vs. $\delta^{18}O_A$ **(d). Solid black circles** represent the average isotopic composition of local snow cover. The isotopic compositions of local vapor fluxes at Mt. Zugspitze ($^*R_V$) for February (**blue**) and May (**red**) vary with changes in h and T_a. **Gray ellipsoids** and **open symbols** represent the same Monte Carlo simulation and data as described in Figure 10, respectively.

Local $^*R_W$ input values for calculating the isotopic composition of the vapor flux are obtained from the average composition of the local snow cover ($\delta^{17}O$=–8.729‰, $\delta^{18}O$=–16.555‰, δD=–122.3‰). Both $^*R_W$ calculated for February and May are identical within analytical uncertainty. Turbulence in the diffusive boundary layer is parametrized with n=0.5. A slightly higher value of n=0.58 is suggested for water droplets and snow particles suspended in air (Stewart 1975; Froehlich et al. 2008). However, it is more likely that prevailing winds induce steady turnover of surface snow but do not necessarily keep it in suspension.

Isotopic fluxes that were calculated for snow evaporation ($^*R_{V\_Feb}$ and $^*R_{V\_May}$) only show a small difference (Fig. 13 c and d) that can be attributed to the different average h and T_a used in the calculation (February: h=0.73±0.05, T_a=–5.9±3 °C; May: h=0.67±0.05, T_a=1.0±3 °C). The isotopic composition of local evaporation, $^*R_V$, represents the isotopic end-member in the local atmospheric vapor balance. Actual $^*R_A$ of the free atmosphere results from mixing of $^*R_V$ and the isotopic composition of vapor in the arriving air mass (Fig. 13 c and d, gray ellipsoids). A higher recycling ratio will shift $^*R_A$ towards the composition of $^*R_V$, whereas low q_R will not change the isotopic composition of arriving vapor significantly. This explains why peak values of ^{17}O-excess$_A$ and d-excess$_A$ coincide with low T_a and $\delta^{18}O_A$, while minimum ^{17}O-excess$_A$ and d-excess$_A$ are associated with higher T_a and $\delta^{18}O_A$ (Fig. 8).

Cold air generally holds lower H_2O concentrations which would, in turn, decrease the contribution of arriving vapor in the local vapor balance, elevating local q_R and, thus, the imprint of the local vapor flux. Some uncertainty may arise from the fact that vapor samples were extracted at ~2.5 m above ground and may—due to insufficient mixing of the diffusive boundary layer—reflect the isotopic composition of the evaporative flux rather than free atmospheric vapor.

FUTURE WORK AND CONCLUSION

Future work

Analytical challenges. It was demonstrated that fluorination of H_2O using a CoF_3 reagent combined with dual-inlet mass spectrometry provides a reasonably good reproducibility (±5 per meg) in ^{17}O-excess to identify small natural variations (Barkan and Luz 2005). Analytical errors (seen as data scatter) in $\delta^{17}O$ and $\delta^{18}O$ are well correlated, thus not affecting the precision for ^{17}O-excess (Landais et al. 2006). A sample memory effect occurring in CoF_3 lines is evident but well corrigible (i.e., by four blind injections between samples with a 55‰ difference in $\delta^{18}O$ (Barkan and Luz 2005)). Mass spectrometric analysis may be affected by unrecognized blanks, leaks, and scale compression. So far, two-point data normalization using VSMOW-2 and SLAP-2 provides an adequate correction (Schoenemann et al. 2013). Still, this normalization has to be extrapolated for samples exceeding $\delta^{18}O = 0‰$ (e.g., waters from arid regions), hence an isotopically enriched standard with a commonly accepted triple oxygen isotope composition would improve inter-laboratory comparison.

In the past years, it has been shown that cavity ring-down spectroscopy provides sufficiently low uncertainty for measuring natural variations in ^{17}O-excess (Berman et al. 2013; Schoenemann et al. 2014; Affolter et al. 2015; Tian et al. 2018). However, water mixing by the autosampler syringe and water adhesion to internal surfaces of the instrument were identified as causes for considerably high memory effects (Berman et al. 2013 and references therein). Three approaches are suggested to minimize these effects: i) preconditioning with blind injections, ii) a mathematical memory correction, and iii) avoiding large differences in isotopic composition of adjacent samples (Schauer et al. 2016). In contrast to mass spectrometric analysis, data scatter in $\delta^{17}O$ and $\delta^{18}O$ is not correlated, thus increasing the uncertainty for ^{17}O-excess (Berman et al. 2013). Still, the improvement of analytical protocols has demonstrated that optical isotope analysis may reach ± 10 per meg uncertainty providing a sample throughput comparable to that of isotope laboratories using the fluorination method (Schauer et al. 2016). In the future, these developments will be crucial for the expansion of spatial coverage and automated long-term observations that will be needed for a global monitoring network of triple oxygen isotopes in precipitation and vapor. Precise knowledge of ^{17}O-excess in atmospheric vapor would e.g., be essential to constrain the evaporative fractionation in lake balance models (Gázquez et al. 2018; Surma et al. 2018; Voigt et al. 2020) and to improve the performance of general circulation models (Steen-Larsen et al. 2016).

Modeling of cloud processes and global transport. In order to improve the understanding of ^{17}O-excess distribution in precipitation and vapor across the globe, adequate prediction using isotope-enabled general circulation models (GCM) is inevitable. The fractionation of water isotopologues (including $H_2{}^{17}O$) was implemented into the LMDZ GCM and extensively tested for variations along latitudinal gradients and seasonal variations (Risi et al. 2013). Accounting for evaporative conditions, Rayleigh distillation, tropospheric vapor mixing, and rain re-evaporation the authors have shown that the sensitivity of ^{17}O-excess to evaporative conditions is apparently underestimated by the model. Schoenemann and Steig (2016) also demonstrated that intermediate complexity modeling (ICM) which accounts for seasonal climatological cycles

(i.e., relative humidity, sea surface temperature, sea ice extent, evaporation, precipitation rate) and diffusivity during low temperature precipitation, captures ^{17}O-excess variations observed in Antarctic precipitation. The authors show that variable moisture source conditions alone cannot explain large seasonal at Vostok/East Antarctica, stressing the importance of local temperature effects on snow formation. It is suggested to apply additional corrections for snow sublimation and 'diamond dust' (clear-sky precipitation) input in interior Antarctica (Casado et al. 2018; Miller 2018; Pang et al. 2019). Improving these parametrizations and the understanding of advection processes during poleward transport of moisture will be critical for triple oxygen isotope based GCM simulations of past climate (e.g., Cauquoin et al. 2019a,b).

In order to improve GCM estimates on spatio-temporal ^{17}O-excess distribution in vapor and precipitation, the coverage of measurements should be drastically improved to provide a profound basis for GCM vs. observation evaluations (Risi et al. 2013; Steen-Larsen et al. 2016). Better knowledge of equilibrium and diffusive solid–vapor fractionation at low temperatures will be necessary to improve GCM capabilities in polar regions. Adequate integration of evaporation from soils and plants will be essential to provide robust estimates on continental moisture recycling (Gat and Matsui 1991; Aemisegger et al. 2014).

Mineral–water systems. ^{17}O-excess studies of ice core records have shown that ^{17}O-excess is a valuable tracer for paleoclimate reconstruction (Guillevic et al. 2014; Landais et al. 2018). However, ice records are mostly restricted to polar areas, emphasizing the need of other triple oxygen isotope records in low- and mid-latitude regions. Recent publications demonstrate a several mineral–water systems that show the capability to capture triple oxygen isotope compositions of ambient water by direct equilibration with mineral-bound oxygen or in hydration water and fluid inclusions.

Speleothems provide a unique climate archive with high temporal resolution for low- and mid-latitudes since they are known to reflect the isotopic composition of regional precipitation (e.g., Bar-Matthews et al. 1996). ^{17}O-excess in meteoric water that was reconstructed from speleothem carbonates is in good agreement with actual precipitation measurements and show significant regional differences between sampling sites (South American and Asian monsoon regions, eastern Mediterranean, China, and Central Asia). The authors explain these variations to different moisture source conditions of regional precipitation (Sha et al. 2020). However, reconstructed moisture source humidity remains mostly constant in those records during glacial-interglacial transitions. Affolter et al. (2015) also present a method for direct ^{17}O-excess measurements on fluid inclusions in speleothem samples, providing a more direct estimate of paleo precipitation without requiring accurate constraints on the isotopic fractionation between water and calcite (Bergel et al. 2020; Fosu et al. 2020; Voarintsoa et al. 2020). However, this approach requires larger sample amounts (0.5–1.5 g of carbonate).

Authigenic lake minerals that form in equilibrium with ambient waters provide another valuable tracer for ^{17}O-excess reconstruction. It was shown shown that isotopic compositions of parent water bodies (i.e., lakes and ponds) can be precisely reconstructed by liberation and analysis of gypsum hydration water, and accurate knowledge of triple oxygen fractionation between the structurally bonded and the ambient water (Gázquez et al. 2015, 2017; Herwartz et al. 2017). Quantitative estimates on local relative humidity changes were made by combining this approach with d-excess measurements to natural samples from lakes in arid regions (Evans et al. 2018; Gázquez et al. 2018). Recent studies also reveal that ^{17}O-excess in lake carbonates reflects the isotopic composition of parent water bodies and primary catchment precipitation (Passey et al. 2014; Passey and Ji 2019; Passey and Levin 2021, this volume). It is also suggested that additional analysis of 'clumped isotopes' (Δ_{47}) is valuable to improve back-projection modeling of parent waters by adding constraints on the carbonate formation temperature (Ghosh et al. 2006; Passey and Ji 2019).

Analysis of triple oxygen isotopes in fine-grained and clay-rich sediments by Bindeman et al. (2019) has also shown that integrated isotope signals of regional precipitation are captured in weathering products of bedrock. Using appropriate fractionation factors for water–clay equilibrium (Bindeman et al. (2019) and references therein) and a model for back-projection of water, mean annual temperatures can be reconstructed. Another application of this approach is the reconstruction of a paleo-GMWL based on the analysis of shales and clay minerals (Bindeman 2021, this volume).

Landais et al. (2006) have demonstrated that $\delta^{17}O$–$\delta^{18}O$ variations in plant leaf water follow a transpiration fractionation trend (λ_{transp}) which is distinctively lower than equilibrium fractionation of water and that λ_{transp} is controlled by ambient relative humidity. Recent studies have shown that phytoliths (amorphous silica microstructures in plants) reflect the triple oxygen isotope composition of leaf water (Alexandre et al. 2018; Alexandre et al. 2019).Assuming constant triple oxygen isotope fractionation between silica and leaf water ($\theta_{Phyto–LW}=0.521$), this approach may provide a unique tracer for paleo-humidity. However, it has yet to be proven that $\theta_{Phyto–LW}$ is climate independent and can thus be applied for reconstructing paleo-leaf water. If so, reconstructed leaf water could provide e.g., insights into humidity conditions and the triple oxygen isotopic composition of plant CO_2 (Alexandre et al. 2019).

Water–rock interaction and bedrock re-equilibration also provide valuable hydrological information for geological periods (i.e., the Precambrian) where other records are rare (Herwartz 2021, this volume). Zakharov et al. (2019b) show that regional meteoric water can be reconstructed from triple oxygen isotope mixing patterns found in Icelandic metamorphic rocks. In studies this approach was used to reconstruct the average $\delta^{18}O$ continental ice during Paleoproterozoic global glaciations (Herwartz et al. 2015; Zakharov et al. 2019a). Modeling the isotopic balance for water–rock interaction of Precambrian cherts provides key information on the isotopic composition of the ancient ocean (Sengupta and Pack 2018; Liljestrand et al. 2020; Zakharov et al. 2021, this volume).

Conclusion

Significant improvement of analytical techniques during the last two decades has triggered the use of triple oxygen isotopes in the hydrological cycle, the investigation of underlying fractionation mechanisms, triple-O-based climate reconstructions, and the comprehension of hydrological processes. A major achievement is understanding the global distribution of triple oxygen isotopes which is described by $\delta'^{17}O=0.528 \cdot \delta'^{18}O + 0.033‰$ and referred to as the GMWL.

Essential isotope fractionation processes operating on the global scale include equilibrium evaporation, diffusion of water vapor, and vapor condensation. Though, diffusion and the Craig and Gordon model are well established for δD and $\delta^{18}O$, the accurate determination of triple oxygen isotope fractionation factors describing the $^{17}O/^{16}O$ and $^{18}O/^{16}O$ distribution for dominating processes marks a major breakthrough. Processes that involve diffusive fractionation, such as evaporation or snow formation at low temperatures produce trends that deviate from this relationship and which are found in extreme environments like remote polar regions (low $\delta^{18}O$) or hyper-arid deserts (high $\delta^{18}O$). However, also waters that fall in the range of intermediate $\delta^{18}O$ values (e.g., mid-latitude precipitation) form local $\delta'^{17}O$–$\delta'^{18}O$ trends that deviate from overall $\lambda^{17}_{GMWL}= 0.528$ and reflect re-evaporation of rain droplets or continental moisture recycling.

The temperature independent ^{17}O-excess parameter is a useful, complementary tool in addition to traditional d-excess for the stable isotope-based assessment of hydrological processes, paleoclimatology and paleohydrology. Its sensitivity to diffusive fractionation makes it a valuable tracer for (paleo-)humidity conditions and locations of moisture source regions. However, it has been demonstrated that second order effects such as distillation at low temperatures and re-evaporation of rain droplets may systematically lower the ^{17}O-excess in the final precipitate.

Similar to the use of d-excess in arid regions, ^{17}O-excess is used for hydrological balancing of evaporative water bodies. Combining both parameters results in a better understanding and parametrization of environmental conditions. The use of lake balance models and adequate constraints of boundary conditions (isotopic composition of inflowing water and atmospheric vapor, wind regime) provides valuable estimates on humidity conditions in arid regions. Analysis of authigenic minerals from lake bodies also demonstrates the potential of ^{17}O-excess for paleoclimate applications.

Studies of precipitation in mid-latitudes suggest that elevated ^{17}O-excess in continental interior cannot be explained by the above-mentioned effects and result from moisture recycling along air trajectories. In this work we demonstrate that ^{17}O-excess of atmospheric vapor provides valuable information on continental moisture recycling. However, no data on triple oxygen isotopes in continental vapor from mid-latitudes were available so far to obtain systematic constraints on this effect.

The investigation of moisture recycling would be greatly improved with larger datasets on both, precipitation records and atmospheric vapor. Measurements of ^{17}O-excess in atmospheric vapor in a high temporal resolution will be necessary to improve the understanding of local meteorological effects on local evaporative fluxes and, thus, the isotopic balance of H_2O in the atmosphere. Triple oxygen isotope analysis holds large potential to constrain isotopic estimates for land-locked water reservoirs that are balanced by local evaporation and sublimation to a large extent.

ACKNOWLEDGEMENTS

The project was funded by the German Research Foundation (DFG, grant no. STA 936/8−1).

REFERENCES

Aemisegger F, Pfahl S, Sodemann H, Lehner I, Seneviratne SI, Wernli H (2014) Deuterium excess as a proxy for continental moisture recycling and plant transpiration. Atmos Chem Phys 14:4029–4054

Affolter S, Häuselmann AD, Fleitmann D, Häuselmann P, Leuenberger M (2015) Triple isotope (δD, δ^{17}O, δ^{18}O) study on precipitation, drip water and speleothem fluid inclusions for a Western Central European cave (NW Switzerland). Quat Sci Rev 127:73–89

Alexandre A, Landais A, Vallet-Coulomb C, Piel C, Devidal S, Pauchet S, Sonzogni C, Couapel M, Pasturel M, Cornuault P, Xin J, Mazur J-C, Prié F, Bentaleb I, Webb E, Chalié F, Roy J (2018) The triple oxygen isotope composition of phytoliths as a proxy of continental atmospheric humidity: insights from climate chamber and climate transect calibrations. Biogeosciences 15: 3223–3241

Alexandre A, Webb E, Landais A, Piel C, Devidal S, Sonzogni C, Couapel M, Mazur J-C, Pierre M, Prié F, Vallet-Coulomb C, Outrequin C, Roy J (2019) Effects of leaf length and development stage on the triple oxygen isotope signature of grass leaf water and phytoliths: insights for a proxy of continental atmospheric humidity. Biogeosciences 16:4613–4625

Angert A, Cappa CD, DePaolo DJ (2004) Kinetic ^{17}O effects in the hydrologic cycle: Indirect evidence and implications. Geochim Cosmochim Acta 68:3487–3495

Araguás-Araguás L, Froehlich K, Rozanski K (2000) Deuterium and oxygen−18 isotope composition of precipitation and atmospheric moisture. Hydrol Process 14:1341–1355

Baker L, Franchi IA, Maynard J, Wright IP, Pillinger CT (2002) A technique for the determination of ^{18}O/^{16}O and ^{17}O/^{16}O isotopic ratios in water from small liquid and solid samples. Anal Chem 74:1665–1673

Bao H, Cao X, Hayles JA (2016) Triple oxygen isotopes: fundamental relationships and applications. Ann Rev Earth Planet Sci 44:463–492

Bar-Matthews M, Ayalon A, Matthews A, Sass E, Halicz L (1996) Carbon and oxygen isotope study of the active water-carbonate system in a karstic Mediterranean cave: Implications for paleoclimateresearch in semiarid regions. Geochim Cosmochim Acta 60:337–347

Barkan E, Luz B (2005) High precision measurements of ^{17}O/^{16}O and ^{18}O/^{16}O ratios in H_2O. Rapid Commun Mass Spectrom 19:3737–3742

Barkan E, Luz B (2007) Diffusivity fractionations of $H_2{}^{16}O/H_2{}^{17}O$ and $H_2{}^{16}O/H_2{}^{18}O$ in air and their implications for isotope hydrology. Rapid Commun Mass Spectrom 21:2999–3005

Bastrikov V, Steen-Larsen HC, Masson-Delmotte V, Gribanov K, Cattani O, Jouzel J, Zakharov V (2014) Continuous measurements of atmospheric water vapour isotopes in western Siberia (Kourovka). Atmos Meas Tech 7:1763–1776
Bergel SJ, Barkan E, Stein M, Affek HP (2020) Carbonate $^{17}O_{excess}$ as a paleo-hydrology proxy: Triple oxygen isotope fractionation between H_2O and biogenic aragonite, derived from freshwater mollusks. Geochim Cosmochim Acta 275:36–47
Berman ESF, Levin NE, Landais A, Li S, Owano T (2013) Measurement of $\delta^{18}O$, $\delta^{17}O$, and ^{17}O-excess in water by off-axis integrated cavity output spectroscopy and isotope ratio mass spectrometry. Anal Chem 85:10392–10398
Bershaw J, Hansen DD, Schauer AJ (2020) Deuterium excess and ^{17}O-excess variability in meteoric water across the Pacific Northwest, USA. Tellus 72B:1773722
Bindeman IN (2021) Triple oxygen isotopes in evolving continental crust, granites, and clastic sediments. Rev Mineral Geochem 86:241–290
Bindeman IN, Bayon G, Palandri J (2019) Triple oxygen isotope investigation of fine-grained sediments from major world's rivers: Insights into weathering processes and global fluxes into the hydrosphere. Earth Planet Sci Lett 528:115851
Bolot M, Legras B, Moyer EJ (2013) Modelling and interpreting the isotopic composition of water vapour in convective updrafts. Atmos Chem Phys 13:7903–7935
Bowen G (2018) The Online Isotopes in Precipitation Calculator, version 3.1. available at: http://www.waterisotopes.org
Bowen GJ, Revenaugh J (2003) Interpolating the isotopic composition of modern meteoric precipitation. Water Resour Res 39:1299
Brenninkmeijer CAM, Röckmann T (1996) Russian doll type cryogenic traps: improved design and isotope separation effects. Anal Chem 68:3050–3053
Cappa CD, Hendricks MB, DePaolo DJ, Cohen RC (2003) Isotopic fractionation of water during evaporation. J Geophys Res 108:4525
Casado M, Cauquoin A, Landais A, Israel D, Orsi A, Pangui E, Landsberg J, Kerstel E, Prie F, Doussin J-F (2016) Experimental determination and theoretical framework of kinetic fractionation at the water vapour-ice interface at low temperature. Geochim Cosmochim Acta 174:54–69
Cauquoin A, Risi C, Vignon É (2019a) Importance of the advection scheme for the simulation of water isotopes over Antarctica by atmospheric general circulation models: A case study for present-day and Last Glacial Maximum with LMDZ-iso. Earth Planet Sci Lett 524:115731
Cauquoin A, Werner M, Lohmann G (2019b) Water isotopes—Climate relationships for the mid-Holocene and preindustrial period simulated with an isotope-enabled version of MPI-ESM. Clim Past 15:1913–1937
Christner E, Kohler M, Schneider M (2017) The influence of snow sublimation and meltwater evaporation on δD of water vapor in the atmospheric boundary layer of central Europe. Atmos Chem Phys 17:1207–1225
Ciais P, Jouzel J (1994) Deuterium and oxygen 18 in precipitation: Isotopic model, including mixed cloud processes. J Geophys Res 99:16703–16803
Craig H (1961) Isotopic Variations in Meteoric Waters. Science 133:1702–1703
Craig H, Gordon L (1965) Deuterium and oxygen 18 variations in the ocean and the marine atmosphere. *In*: Stable Isotopes in Oceanographic Studies and Paleotemperatures. Tongiorgi E (ed). Laboratorio di Geologia Nucleare, Pisa, p 9–130
Criss RE (1999) Principles of Stable Isotope Distribution. Oxford University Press, New York
Dansgaard W (1954) The O^{18}-abundance in fresh water. Geochim Cosmochim Acta 6:241–260
Dansgaard W (1964) Stable isotopes in precipitation. Tellus 16:436–468
Dongmann G, Nürnberg HW, Förstel H, Wagener K (1974) On the enrichment of $H_2{}^{18}O$ in the leaves of transpiring plants. Radiat Environ Biophys 11:41–52
Dütsch M, Pfahl S, Meyer M, Wernli H (2018) Lagrangian process attribution of isotopic variations in near-surface water vapour in a 30-year regional climate simulation over Europe. Atmos Chem Phys 18:1653–669
Ehhalt D, Knott K (1965) Kinetische Isotopentrennung bei der Verdampfung von Wasser. Tellus 17:389–397
El Amraoui L, Peuch V-H, Ricaud P, Massart S, Semane N, Teyssèdre H, Cariolle D, Karcher F (2018) Ozone loss in the 2002 - 2003 Arctic vortex deduced from the assimilation of Odin/SMR O_3 and N_2O measurements: N2O as a dynamical tracer. Q J R Meteorol Soc 134:217–228
Ellehoj MD, Steen-Larsen HC, Johnsen SJ, Madsen MB (2013) Ice-vapor equilibrium fractionation factor of hydrogen and oxygen isotopes: Experimental investigations and implications for stable water isotope studies. Rapid Commun Mass Spectrom 27:2149–2158
Evans NP, Bauska TK, Gázquez-Sánchez F, Brenner M, Curtis JH, Hodell DA (2018) Quantification of drought during the collapse of the classic Maya civilization. Science 361:498–501
Fontes JC, Gonfiantini R (1967) Comportement isotopique au cours de l'evaporation de deux bassins sahariens. Earth Planet Sci Lett 3:258–266
Fosu BR, Subba R, Peethambaran R, Bhattacharya SK, Ghosh P (2020) Technical Note: Developments and applications in triple oxygen isotope analysis of carbonates. ACS Earth Space Chem 4:702–710
Franz P, Röckmann T (2005) High-precision isotope measurements of $H_2{}^{16}O$, $H_2{}^{17}O$, $H_2{}^{18}O$, and the $\Delta^{17}O$-anomaly of water vapor in the southern lowermost stratosphere. Atmos Chem Phys 5:2949–2959
Friedman I (1953) Deuterium content of natural waters and other substances. Geochim Cosmochim Acta 4:89–103
Friedman I, Benson C, Gleason J (1991) Isotopic changes during snow metamorphism. *In*: Stable Isotope Geochemistry: A Tribute to Samuel Epstein. Taylor Jr HP, O'Neil JR, Kaplan IR (eds) Geochemical Society, San Antonio p 211–221

Froehlich K, Kralik M, Papesch W, Rank D, Scheifinger H, Stichler W (2008) Deuterium excess in precipitation of Alpine regions - Moisture recycling. Isotopes Environ Health Stud 44:1–10

Gat JR (1984) The stable isotope composition of Dead Sea waters. Earth Planet Sci Lett 71:361–376

Gat JR (1996) Oxygen and hydrogen isotopes in the hydrologic cycle. Ann Rev Earth Planet Sci 24:225–262

Gat JR, Bowser C (1991) The heavy isotope enrichment of water in coupled evaporative systems. *In*: Stable Isotope Geochemistry: A Tribute to Samuel Epstein. Taylor Jr HP, O'Neil JR, Kaplan, IR (eds) Geochemical Society, San Antonio p 159–169.

Gat JR, Matsui E (1991) Atmospheric water balance in the Amazon Basin: an isotopic evapotranspiration model. J Geophys Res 96:13,179–13,188

Gat JR, Mook WG, Meijer HAJ (2000) Volume II: Atmospheric water. *In*: Environmental Isotopes in the Hydrological Cycle. Mook WG (ed) UNESCO, Paris

Gázquez F, Mather I, Rolfe J, Evans NP, Herwartz D, Staubwasser M, Hodell DA (2015) Simultaneous analysis of $^{17}O/^{16}O$, $^{18}O/^{16}O$ and $^{2}H/^{1}H$ of gypsum hydration water by cavity ring-down laser spectroscopy. Rapid Commun Mass Spectrom 29:1997–2006

Gázquez F, Evans NP, Hodell DA (2017) Precise and accurate isotope fractionation factors ($\alpha^{17}O$, $\alpha^{18}O$ and αD) for water and $CaSO_4{\cdot}2H_2O$ (gypsum). Geochim Cosmochim Acta 198:259–270

Gázquez F, Morellón M, Bauska T, Herwartz D, Surma J, Moreno A, Staubwasser M, Valero-Garcés B, Delgado-Huertas A, Hodell DA (2018) Triple oxygen and hydrogen isotopes of gypsum hydration water for quantitative paleo-humidity reconstruction. Earth Planet Sci Lett 481:177–188

Ghosh P, Adkins J, Affek H, Balta B, Guo W, Schauble EA, Schrag D, Eiler JM (2006) $^{13}C–^{18}O$ bonds in carbonate minerals: A new kind of paleothermometer. Geochim Cosmochim Acta 70:1439–1456

Gonfiantini R (1986) Environmental isotopes in lake studies. *In*: Handbook of Environmental Isotope Geochemistry. Fritz P, Fontes J-Ch (eds) Elsevier, Amsterdam p 119–168

Gonfiantini R, Wassenaar LI, Araguas-Araguas L (2020) Stable isotope fractionations in the evaporation of water: The wind effect. Hydrol Process 1–12

Guillevic M, Bazin L, Landais A, Stowasser C, Masson-Delmotte V, Blunier T, Eynaud F, Falourd S, Michel E, Minster B, Popp T, Prié F, Vinther BM (2014) Evidence for a three-phase sequence during Heinrich Stadial 4 using a multiproxy approach based on Greenland ice core records. Clim Past 10:2115–2133

Haese B, Werner M, Lohmann G (2013) Stable water isotopes in the coupled atmosphere–land surface model ECHAM5-JSBACH. Geosci Model Dev 6:1463–1480

Hausmann P, Sussmann R, Trickl T, Schneider M (2017) A decadal time series of water vapor and D/H isotope ratios above Zugspitze: transport patterns to central Europe. Atmos Chem Phys 17:7635–7651

He H, Smith RB (1999) Stable isotope composition of water vapor in the atmospheric boundary layer above the forests of New England. J. Geophys Res Atmos 104:11657–11673

Herwartz D (2021) Triple oxygen isotopes variations in Earth's crust. Rev Mineral Geochem 86:291–322

Herwartz D, Pack A, Krylov D, Xiao Y, Muehlenbachs K, Sengupta S, Di Rocco T (2015) Revealing the climate of snowball Earth from $\Delta^{17}O$ systematics of hydrothermal rocks. PNAS 112:5337–5341

Herwartz D, Surma J, Voigt C, Assonov S, Staubwasser M (2017) Triple oxygen isotope systematics of structurally bonded water in gypsum. Geochim Cosmochim Acta 209:254–266

Horita J, Wesolowski DJ (1994) Liquid–vapor fractionation of oxygen and hydrogen isotopes of water from the freezing to the critical temperature. Geochim Cosmochim Acta 58:3425–3437

Horita J, Rozanski K, Cohen S (2008) Isotopes in environmental and health studies isotope effects in the evaporation of water: a status report of the Craig–Gordon model. Isotopes Environ Health Stud 44:23–49

Hürkamp K, Zentner N, Reckerth A, Weishaupt S, Wetzel KF, Tschiersch J, Stumpp C (2019) Spatial and temporal variability of snow isotopic composition on Mt. Zugspitze, Bavarian Alps, Germany. J Hydrol Hydromechanics 67:49–58

Jasechko S, Sharp ZD, Gibson JJ, Birks SJ, Yi Y, Fawcett PJ (2013) Terrestrial water fluxes dominated by transpiration. Nature 496:347–350

Johnsen SJ, Dansgaard W, White JWC (1989) The origin of Arctic precipitation under present and glacial conditions. Tellus 41B:452–468

Jouzel J, Merlivat L (1984) Deuterium and oxygen 18 in precipitation: modeling of the isotopic effects during snow formation. J Geophys Res 89:11749–11757

Kaiser A, Scheifinger H, Kralik M, Papesch W, Rank D, Stichler W (2002) Links between meteorological conditions and spatial/temporal variations in long-term isotope records from the Austrian precipitation network. International conference on study of environmental change using isotope techniques, IAEA-CN–80/63

Kaiser J (2008) Reformulated ^{17}O correction of mass spectrometric stable isotope measurements in carbon dioxide and a critical appraisal of historic 'absolute' carbon and oxygen isotope ratios. Geochim Cosmochim Acta 72:1312–1334

Kneifel S, Redl S, Orlandi E, Löhnert U, Cadeddu MP, Turner DD, Chen M-T (2014) Absorption properties of supercooled liquid water between 31 and 225 GHz: evaluation of absorption models using ground-based observations. J Appl Meteorol Climatol 53:1028–1045

Kusakabe M, Matsuhisa Y (2008) Oxygen three-isotope ratios of silicate reference materials determined by direct comparison with VSMOW-oxygen. Geochem J 42:309–317

Landais A, Barkan E, Yakir D, Luz B (2006) The triple isotopic composition of oxygen in leaf water. Geochim Cosmochim Acta 70:4105–4115

Landais A, Barkan E, Luz B (2008) Record of $\delta^{18}O$ and ^{17}O-excess in ice from Vostok Antarctica during the last 150,000 years. Geophys Res Lett 35:L02709

Landais A, Risi C, Bony S, Vimeux F, Descroix L, Falourd S, Bouygues A (2010) Combined measurements of $^{17}O_{excess}$ and d-excess in African monsoon precipitation: Implications for evaluating convective parameterizations. Earth Planet Sci Lett 298:104–112

Landais A, Ekaykin A, Barkan E, Winkler R, Luz B (2012a) Seasonal variations of ^{17}O-excess and d-excess in snow precipitation at Vostok station, East Antarctica. J Glaciol 58:725–733

Landais A, Steen-Larsen HC, Guillevic M, Masson-Delmotte V, Vinther B, Winkler R (2012b) Triple isotopic composition of oxygen in surface snow and water vapor at NEEM (Greenland). Geochim Cosmochim Acta 77:304–316

Landais A, Capron E, Toucanne S, Rhodes R, Popp T, Vinther B, Minster B, Prié F (2018) Ice core evidence for decoupling between midlatitude atmospheric water cycle and Greenland temperature during the last deglaciation. Clim Past 14:1405–1415

Lawrence DM, Thornton PE, Oleson KW, Bonan GB (2007) The partitioning of evapotranspiration into transpiration, soil evaporation, and canopy evaporation in a GCM: Impacts on land–atmosphere interaction. J Hydrometeorol 8:862–880

Li S, Levin NE, Chesson LA (2015) Continental scale variation in ^{17}O-excess of meteoric waters in the United States. Geochim Cosmochim Acta 164:110–126

Li S, Levin NE, Soderberg K, Dennis KJ, Caylor KK (2017) Triple oxygen isotope composition of leaf waters in Mpala, central Kenya. Earth Planet Sci Lett 468:38–50

Liljestrand FL, Knoll AH, Tosca NJ, Cohen PA, Macdonald FA, Peng Y, Johnston DT (2020) The triple oxygen isotope composition of Precambrian chert. Earth Planet Sci Lett 537:116167

Lin Y, Clayton RN, Huang L, Nakamura N, Lyons JR (2013a) Oxygen isotope anomaly observed in water vapor from Alert, Canada and the implication for the stratosphere. PNAS 110:15,608–15,613

Lin Y, Clayton RN, Huang L, Nakamura N, Lyons JR (2013b) Reply to Miller: Concerning the oxygen isotope anomaly observed in water vapor from Alert, Canada, and its stratospheric source. PNAS 110:E4568

Lohmann U, Henneberger J, Henneberg O, Fugal JP, Bühl J, Kanji ZA (2016) Persistence of orographic mixed-phase clouds. Geophys Res Lett 43:10,512–10,519

Lowenthal D, Hallar AG, McCubbin I, David R, Borys R, Blossey P, Muhlbauer A, Kuang Z, Moore M (2016) Isotopic fractionation in wintertime orographic clouds. J Atmos Oceanic Technol 33:2663–2678

Luz B, Barkan E (2010) Variations of $^{17}O/^{16}O$ and $^{18}O/^{16}O$ in meteoric waters. Geochim Cosmochim Acta 74:6276–6286

Luz B, Barkan E, Yam R, Shemesh A (2009) Fractionation of oxygen and hydrogen isotopes in evaporating water. Geochim Cosmochim Acta 73:6697–6703

Majoube M (1971) Fractionnement en oxygène 18 entre la glace et la vapeur d'eau. J Clim Phys 68:625–636

Masson-Delmotte V, Jouzel J, Landais A, Stievenard M, Johnsen SJ, White JWC., Werner M, Sveinbjornsdottir A, Fuhrer K (2005) GRIP deuterium excess reveals rapid and orbital-scale changes in Greenland moisture origin. Science 309:118–121

Mathieu R, Bariac T (1996) A numerical model for the simulation of stable isotope profiles in drying soils. J Geophys Res 101:12,685–12,696

Meijer HAJ, Li WJ (1998) The use of electrolysis for accurate $\delta^{17}O$ and $\delta^{18}O$ isotope measurements in water. Isotopes Environ Health Stud 34:349–369

Merlivat L (1978) Molecular diffusivities of $H_2{}^{16}O$, $HD^{16}O$, and $H_2{}^{18}O$ in gases. J Chem Phys 69:2864–2871

Merlivat L, Nief G (1967) Fractionnement isotopique lors des changements d'état solide–vapeur et liquide–vapeur de l'eau à des températures inférieures à 0°C. Tellus 19:122–127

Merlivat L, Jouzel J (1979) Global climatic interpretation of the deuterium–oxygen 18 relationship for precipitation. J Geophys Res 84:5029–5033

Miller MF (2013) Oxygen isotope anomaly not present in water vapor from Alert, Canada. PNAS 110:E4567

Miller MF (2018) Precipitation regime influence on oxygen triple-isotope distributions in Antarctic precipitation and ice cores. Earth Planet Sci Lett 481:316–327

NorthGRIP Members (2004) High-resolution record of Northern Hemisphere climate extending into the last interglacial period. Nature 431:147–151

Pang H, Hou S, Landais A, Masson-Delmotte V, Jouzel J, Steen-Larsen HC, Risi C, Zhang W, Wu S, Li Y, An C, Wang Y, Prie F, Minster B, Falourd S, Stenni B, Scarchilli C, Fujita K, Grigioni P (2019) Influence of summer sublimation on δD, $\delta^{18}O$, and $\delta^{17}O$ in precipitation, East Antarctica, and implications for climate reconstruction from ice cores. J Geophys Res Atmos 124:7339–7358

Passey BH, Ji H (2019) Triple oxygen isotope signatures of evaporation in lake waters and carbonates: A case study from the western United States. Earth Planet Sci Lett 518:1–12

Passey BH, Levin NE (2021) Triple oxygen isotopes in meteoric waters, carbonates, and biological apatites: implications for continental paleoclimate reconstruction. Rev Mineral Geochem 86:429–462

Passey BH, Hu H, Ji H, Montanari S, Li S, Henkes GA, Levin NE (2014) Triple oxygen isotopes in biogenic and sedimentary carbonates. Geochim Cosmochim Acta 141:1–25

Peng H, Mayer B, Norman A-L, Krouse HR (2005) Modelling of hydrogen and oxygen isotope compositions for local precipitation. Tellus 57B:273–282

Petit JR, Jouzel J, Raynaud D, Barkov NI, Barnola J-M, Basile I, Bender M, Chappellaz J, Davis M, Delaygue G, Delmotte M, Kotlyakov VM, Legrand M, Lipenkov VY, Lorius C, Pépin L, Ritz C, Saltzman E, Stievenard M (1999) Climate and atmospheric history of the past 420,000 years from the Vostok ice core, Antarctica. Nature 399:429–436

Pfahl S, Sodemann H (2014) What controls deuterium excess in global precipitation? Clim Past 10:771–781

Pfahl S, Wernli H (2008) Air parcel trajectory analysis of stable isotopes in water vapor in the eastern Mediterranean. J Geophys Res Atmos 113:D20104

Risi C, Landais A, Winkler R, Vimeux F (2013) Can we determine what controls the spatio-temporal distribution of d-excess and ^{17}O-excess in precipitation using the LMDZ general circulation model? Clim Past 9:2173–2193

Rozanski BK, Sonntag C, Münnich K (1982) Factors controlling stable isotope composition of European precipitation. Tellus 34:142–150

Schauer AJ, Schoenemann SW, Steig EJ (2016) Routine high-precision analysis of triple water-isotope ratios using cavity ring-down spectroscopy. Rapid Commun Mass Spectrom 30:2059–2069

Schlaepfer DR, Ewers BE, Shuman BN, Williams DG, Frank JM, Massman WJ, Lauenroth WK (2014) Terrestrial water fluxes dominated by transpiration: Comment. Ecosphere 5:61

Schoenemann SW, Steig EJ (2016) Seasonal and spatial variations of $^{17}O_{excess}$ and d_{excess} in Antarctic precipitation: Insights from an intermediate complexity isotope model. J Geophys Res Atmos 121:11,215–11,247

Schoenemann SW, Schauer AJ, Steig EJ (2013) Measurement of SLAP2 and GISP δ^{17}O and proposed VSMOW-SLAP normalization for δ^{17}O and $^{17}O_{excess}$. Rapid Commun Mass Spectrom 27:582–590

Schoenemann SW, Steig EJ, Ding Q, Markle BR, Schauer AJ (2014) Triple water-isotopologue record from WAIS Divide, Antarctica: Controls on glacial-interglacial changes in $^{17}O_{excess}$ of precipitation. J Geophys Res Atmos 119:8741–8763

Sengupta S, Pack A (2018) Triple oxygen isotope mass balance for the Earth's oceans with application to Archean cherts. Chem Geol 495:18–26

Sha L, Mahata S, Duan P, Luz B, Zhang P, Baker J, Zong B, Ning Y, Brahim YA, Zhang H, Edwards RL, Cheng H (2020) A novel application of triple oxygen isotope ratios of speleothems. Geochim Cosmochim Acta 270:360–378

Sharp ZD, Gibbons JA, Maltsev O, Atudorei V, Pack A, Sengupta S, Shock EL, Knauth LP (2016) A calibration of the triple oxygen isotope fractionation in the SiO_2–H_2O system and applications to natural samples. Geochim Cosmochim Acta 186:105–119

Sodemann H, Zubler E (2010) Seasonal and inter-annual variability of the moisture sources for Alpine precipitation during 1995–2002. Int J Climatol 30:947–961

Steen-Larsen HC, Masson-Delmotte V, Sjolte J, Johnsen SJ, Vinther BM, Bréon FM, Clausen HB, Dahl-Jensen D, Falourd S, Fettweis X, Gallée H, Jouzel J, Kageyama M, Lerche H, Minster B, Picard G, Punge HJ, Risi C, Salas D, Schwander J, Steffen K, Sveinbjörnsdóttir AE, Svensson A, White J (2011) Understanding the climatic signal in the water stable isotope records from the NEEM shallow firn/ice cores in northwest Greenland. J Geophys Res Atmos 116:D06108

Steen-Larsen HC, Risi C, Werner M, Yoshimura K, Masson-Delmotte V (2016) Evaluating the skills of isotope-enabled general circulation models against in situ atmospheric water vapor isotope observations. J Geophys Res 122:246–263

Steen-Larsen HC, Sveinbjörnsdottir AE, Peters AJ, Masson-Delmotte V, Guishard MP, Hsiao G, Jouzel J, Noone D, Warren JK, White JWC (2014) Climatic controls on water vapor deuterium excess in the marine boundary layer of the North Atlantic based on 500 days of in situ, continuous measurements. Atmos Chem Phys 14:7741–7756

Steig EJ, Gkinis V, Schauer AJ, Schoenemann SW, Samek K, Hoffnagle J, Dennis KJ, Tan SM (2014) Calibrated high-precision ^{17}O-excess measurements using cavity ring-down spectroscopy with laser-current-tuned cavity resonance. Atmos Meas Tech 7:2421–2435

Stein AF, Draxler RR, Rolph GD, Stunder BJB, Cohen MD, Ngan F (2015) NOAA's HYSPLIT Atmospheric Transport and Dispersion Modeling System. Bull Am Meteorol Soc 90:2059–2077

Stewart MK (1975) Stable Isotope Fractionation Due to Evaporation and Isotopic Exchange of Falling Waterdrops: Applications to Atmospheric Processes and Evaporation of Lakes. J Geophys Res 80:1133–1146

Strasser U, Bernhardt M, Weber M, Liston GE, Mauser W (2008) Is snow sublimation important in the alpine water balance? Cryosphere 2:53–66

Stumpp C, Klaus J, Stichler W (2014) Analysis of long-term stable isotopic composition in German precipitation. J Hydrol 517:351–361

Surma J, Assonov S, Bolourchi MJ, Staubwasser M (2015) Triple oxygen isotope signatures in evaporated water bodies from the Sistan Oasis, Iran. Geophys Res Lett 42:8456–8462

Surma J, Assonov S, Herwartz D, Voigt C, Staubwasser M (2018) The evolution of ^{17}O-excess in surface water of the arid environment during recharge and evaporation. Sci Rep 8:4972

Tian C, Wang L, Novick KA (2016) Water vapor δ^2H, δ^{18}O and δ^{17}O measurements using an off-axis integrated cavity output spectrometer—sensitivity to water vapor concentration, delta value and averaging-time. Rapid Commun Mass Spectrom 30:2077–2086

Tian C, Wang L, Kaseke KF, Bird BW (2018) Stable isotope compositions (δ^2H, δ^{18}O and δ^{17}O) of rainfall and snowfall in the central United States. Sci Rep 8:6712

Tian C, Wang L, Tian F, Zhao S, Jiao W (2019) Spatial and temporal variations of tap water ^{17}O-excess in China. Geochim Cosmochim Acta 260:1–14

Touzeau A, Landais A, Stenni B, Uemura R, Fukui K, Fujita S, Guilbaud S, Ekaykin A, Casado M, Barkan E, Luz B, Magand O, Teste G, Le Meur E, Baroni M, Savarino J, Bourgeois I, Risi C (2016) Acquisition of isotopic composition for surface snow in East Antarctica and the links to climatic parameters. Cryosphere 10:837–852

Trenberth KE (1999) Atmospheric moisture recycling: role of advection and local evaporation. J Clim 12:1368–1381

Trenberth KE, Smith L, Qian T, Dai A, Fasullo J (2007) Estimates of the global water budget and its annual cycle using observational and model data. J Hydrometeorol 8:758–769

Trickl T, Feldmann H, Kanter H-J, Scheel H-E, Sprenger M, Stohl A, Wernli H (2010) Forecasted deep stratospheric intrusions over Central Europe: Case studies and climatologies. Atmos Chem Phys 10:499–524

Uechi Y, Uemura R (2019) Dominant influence of the humidity in the moisture source region on the ^{17}O-excess in precipitation on a subtropical island. Earth Planet Sci Lett 513:20–28

Uemura R, Barkan E, Abe O, Luz B (2010) Triple isotope composition of oxygen in atmospheric water vapor. Geophys Res Lett 37:L04402

van der Ent RJ, Savenije HHG, Schaefli B, Steele-Dunne SC (2010) Origin and fate of atmospheric moisture over continents. Water Resour Res 46:W09525

Van Hook WA (1968) Vapor pressures of the isotopic waters and ices. J Phys Chem 72:1234–1244

Vimeux F, Masson V, Jouzel J, Stievenard M, Petit JR (1999) Glacial–interglacial changes in ocean surface conditions in the Southern Hemisphere. Nature 398:410–413

Voarintsoa NRG, Barkan E, Bergel S, Vieten R, Affek HP (2020) Triple oxygen isotope fractionation between $CaCO_3$ and H_2O in inorganically precipitated calcite and aragonite. Chem Geol 539:119500

Vogelmann H, Sussmann R, Trickl T, Reichert A (2015) Spatiotemporal variability of water vapor investigated using lidar and FTIR vertical soundings above the Zugspitze. Atmos Chem Phys 15:3135–3148

Voigt C, Herwartz D, Dorador C, Staubwasser M (2020) Triple oxygen isotope systematics of evaporation and mixing processes in a dynamic desert lake system. Hydrol Earth Syst Sci Discuss in review

Wang XF, Yakir D (2000) Using stable isotopes of water in evapotranspiration studies. Hydrol Process 14:1407–1421

Wei Z, Lee X (2019) The utility of near-surface water vapor deuterium excess as an indicator of atmospheric moisture source. J Hydrol 577:123923

Welp LR, Lee X, Griffis TJ, Wen X-F, Xiao W, Li S, Sun X, Hu Z, Val Martin M, Huang J (2012) A meta-analysis of water vapor deuterium-excess in the midlatitude atmospheric surface layer. Global Biogeochem Cycles 26:GB3021

Winkler R, Landais A, Risi C, Baroni M, Ekaykin A, Jouzel J, Petit JR, Prie F, Minster B, Falourd S (2013) Interannual variation of water isotopologues at Vostok indicates a contribution from stratospheric water vapor. PNAS 110:17674–17679

Winkler R, Landais A, Sodemann H, Dümbgen L, Prié F, Masson-Delmotte V, Stenni B, Jouzel J (2012) Deglaciation records of ^{17}O-excess in East Antarctica: reliable reconstruction of oceanic normalized relative humidity from coastal sites. Clim Past 8:1–16

Wostbrock JAG, Sharp ZD, Sanchez-Yanez C, Reich M, van den Heuvel DB, Benning LG (2018) Calibration and application of silica-water triple oxygen isotope thermometry to geothermal systems in Iceland and Chile. Geochim Cosmochim Acta 234:84–97

Yu W, Tian L, Ma Y, Xu B, Qu D (2015) Simultaneous monitoring of stable oxygen isotope composition in water vapour and precipitation over the central Tibetan Plateau. Atmos Chem Phys 15:10,251–10,262

Zakharov DO, Bindeman IN, Serebryakov NS, Prave AR, Azimov PY, Babarina II (2019a) Low $\delta^{18}O$ rocks in the Belomorian belt, NW Russia, and Scourie dikes, NW Scotland: A record of ancient meteoric water captured by the early Paleoproterozoic global mafic magmatism. Precambrian Res 333:105431

Zakharov DO, Bindeman IN, Tanaka R, Friðleifsson GÓ, Reed MH, Hampton RL (2019b) Triple oxygen isotope systematics as a tracer of fluids in the crust: A study from modern geothermal systems of Iceland. Chem Geol 530:119312

Zakharov DO, Marin-Carbonne J, Alleon J, Bindeman, IN (2021) Temporal triple oxygen isotope trend recorded by Precambrian cherts: A perspective from combined bulk and in situ secondary ion probe measurements. Rev Mineral Geochem 86:323–365